This is a preprint, the final version is subject to change, of the American Mineralogist (MSA)
Cite as Authors (Year) Title. American Mineralogist, in press.
DOI: https://doi.org/10.2138/am-2019-7116

REVISION 1

REE-, Sr- Ca-aluminum-phosphate-sulfate minerals of the alunite supergroup and their role as hosts for radionuclides

Nicholas D. Owen[1,2,*], Nigel J. Cook[1], Mark Rollog[1], Kathy J. Ehrig[3], Danielle S. Schmandt[1], Rahul Ram[2], Joël Brugger[2], Cristiana L. Ciobanu[1], Benjamin Wade[4], Paul Guagliardo[5]

[1]*School of Chemical Engineering, The University of Adelaide, SA 5005, Australia*

[2]*School of Earth and Environmental Sciences, Monash University, VIC 2800, Australia*

[3]*BHP Olympic Dam, Adelaide, SA 5000, Australia*

[4]*Adelaide Microscopy, The University of Adelaide, SA 5005, Australia*

[5]*Centre for Microscopy, Characterisation, and Analysis, University of Western Australia, 35 Stirling Highway, Crawley, WA 6009, Australia*

ABSTRACT

Aluminum-phosphate-sulfate (APS) minerals of the alunite supergroup are minor components of uranium-bearing copper ores from the Olympic Dam deposit, South Australia. They typically represent a family of paragenetically-late replacement phases after pre-existing REE-bearing phosphates (fluorapatite, monazite, and xenotime). Characterization with respect to textures and composition allows two groups to be distinguished: Ca-Sr-dominant APS minerals that fall within the woodhouseite and svanbergite compositional fields; and a second REE- and phosphate-dominant group closer to florencite in composition. All phases nevertheless display extensive solid solution among end-members in the broader APS clan and show extensive compositional zoning at the grain-scale. Samples representative

* Corresponding author. e-mail address: nicholas.owen@adelaide.edu.au

of the deposit (flotation concentrate and tailings), as well as those which have been chemically altered during the processing cycle (acid leached concentrate) were studied for comparison. NanoSIMS isotope mapping provides evidence that the APS minerals preferentially scavenge and incorporate daughter radionuclides of the ^{238}U decay chain, notably ^{226}Ra and ^{210}Pb, both over geological time within the deposit and during ore processing. These data highlight the role played by minor phases as hosts for geologically mobile deleterious components in ores as well as during mineral processing. Moreover, Sr-Ca-dominant APS minerals exhibit preferential sorption of Pb from fluid sources, in the form of both common Pb and ^{210}Pb, for the first time revealing potential pathways for ^{210}Pb elimination and reduction from ore processing streams.

Keywords: Alunite supergroup; aluminum-phosphate-sulfates; Olympic Dam; ^{238}U decay series radionuclides; mineral processing.

INTRODUCTION

Minerals of the alunite supergroup (Jambor 1999; Bayliss et al. 2010), especially the beudantite and crandallite groups, have found extensive application in environmental remediation and storage of deleterious elements due to their broad stability and their capacity to host a wide range of contaminants via extensive solid solution with the exchange of bi- to hexavalent cations at multiple sites in their structures (Kolitsch and Pring 2001). Elements that can be incorporated include As, Pb, Bi, Hg, Tl, Sb, Cr, Se, and rare earth elements (REE) (Kolitsch and Pring 2001), as well as radioisotopes generated by decay of radioactive K, Sr, Th and U (Dymkov et al. 1997; Kolitsch and Pring 2001). Analysis of APS mineral compositions can reveal useful information regarding local conditions of formation with respect to fluid composition, pH and f_{O_2} (Schwab et al. 2004, 2005; Gaboreau et al. 2007).

Most beudantite- and crandallite-group minerals are stable up to high temperatures (400-500 °C) and remain insoluble even over a wide range of pH and E_h conditions (Kolitsch and Pring 2001). These robust

characteristics also make them potential hosts for daughter products of U decay (notably the radionuclides ^{210}Pb and ^{210}Po, hereafter ^{210}RN) in U-bearing ore deposits and in materials resulting from the processing of such ores.

Hydrothermal REE-, Ca- and/or Sr-bearing aluminum phosphate-sulfate (APS) phases of varied composition within the alunite supergroup are reported from the giant ca. 1590 Ma (Johnson and Cross 1995) Olympic Dam Cu-U-Au-Ag deposit, South Australia (Ehrig et al. 2012). Until now, however, these phases have been inadequately characterized and despite their textural and compositional complexity, were generically categorized as 'crandallite group' minerals with the general formula $(Ce,La,Nd,Ca,Sr)(Al,Fe)_3(SO_4,PO_4)_2(OH)_6$. These minerals are only present in modest amounts (modal abundance 0.109 wt.%), yet are long suspected of making at least a minor contribution to the budget of U and REE in the ore (Ehrig et al. 2012).

Given their ability to incorporate a wide range of radioactive decay products, the presence of Ca- and Sr-bearing APS minerals within a uranium-bearing ore, such as Olympic Dam, makes them a viable host for transport of ^{210}RN throughout the processing cycle. This study sets out to document APS minerals from Olympic Dam with respect to their composition, paragenetic position, relationships with other minerals, and not least their potential role as natural mineral sinks for the products of radioactive decay. Evidence for uptake and incorporation of radionuclides (RN) via both geological processes *in situ* within the deposit and during ore processing (flotation and subsequent acid leaching) is presented and discussed.

BACKGROUND

APS crystal chemistry

APS minerals of the alunite supergroup have the general formula $[AB_3(XO_4)_2(OH)_6]$, where A is a mono-, bi-, or trivalent cation, B is a trivalent cation (in this case almost exclusively Al^{3+}), and XO_4 is mainly a mixture of phosphate and sulfate groups. They are known to form in a variety of geological

environments from weathering profiles in soils, sedimentary settings (Triplehorn et al. 1991; Rasmussen 1996; Pe-Piper and Dolansky 2005) to magmatic-hydrothermal ore deposits such as the Olympic Dam Cu-U-Au-Ag deposit discussed here (Ehrig et al. 2012). The alunite supergroup contains minerals with an extensive and diverse range of compositions. Almost all crystallize within the *R3m* or $R\bar{3}m$ space groups and thus have almost identical crystal structures, albeit with slight deviation of lattice parameters, thus opening up the possibility of extensive solid solution across the APS group.

The crystal structure of APS minerals (Fig. 1) are built up of sheets of AlO_6 octahedra arranged in a Kagomé network perpendicular to the parallel to the (001) plane (Kato and Miura 1977), and two phosphate and/or sulfate tetrahedra, with the A-site cation sitting in between layers (e.g. Schwab et al. 2004, 2005; Zema et al. 2012). To form the sheets, AlO_6 octahedra, with four hydroxyl groups and two oxygen ligands, corner-share hydroxyl groups with one another forming large hexagonal and small trigonal rings. The 'base' of each phosphate or sulfate tetrahedra then shares three corners each of the trigonal rings, forming an overall structure in which two corners of each AlO_6 octahedra and three corners of each phosphate/sulfate tetrahedra, are made of shared oxygen atoms. Peaks formed by the remaining oxygen atom in each phosphate/sulfate tetrahedra then point in alternating sequence in the direction parallel to the *c* axis, into the hexagonal rings formed by AlO_6 octahedra in adjacent layers above and below (Kato and Miura 1977; Gaboreau and Vieillard 2004; Schwab et al. 2004, 2005). The resulting overall structure contains 12-, 6- and 4-fold coordination positions, allowing cations of various charge and radius to fit within the structure (Schwab et al. 2004), aiding in the development of extensive solid solutions occurring in nature. A-site cations generally sit within the 12-fold coordination position but disordering of cations among these positions has been recorded, resulting in a small lowering of symmetry to the monoclinic *Cm* and *C2/m* space groups (Kolitsch and Pring 2001).

Olympic Dam

The Olympic Dam mining-processing-smelting-refining operation exploits a complex, fine-grained sulfide-rich copper ore dominated by hematite, by far the most abundant gangue mineral (Ehrig et al. 2012). Economic commodities are Cu, U, Au and Ag but the IOCG-U-Ag deposit also contains anomalous concentrations of rare earth elements (REE), P, Th, F and many other elements. More than 100 minerals have been identified in the ore, necessitating a thorough understanding and careful control of ore mineralogy to ensure optimized processing.

In the Olympic Dam ore, the four most significant U-bearing minerals are uraninite, coffinite, brannerite and hematite (Ehrig et al. 2012; Ciobanu et al. 2013; Macmillan et al. 2016, 2017; Verdugo-Ihl et al. 2017; Xing et al. 2018). Uranium is extracted by acid leaching of both flotation tails and flotation concentrates. In the ore, U-minerals occur intimately intergrown within mineral assemblages also containing the other economic metals Cu, Ag and Au. Decay of the most common isotope of uranium, ^{238}U, generates daughter isotopes ^{226}Ra, ^{210}Pb and ^{210}Po, which, due to their relatively short half-lives (1,600 years, ~22.2 years and 138.4 days, respectively), have high activities, yet remain active for relatively long times, at least on the human time scale. As a result, the presence of these isotopes in concentrates represent cause for concern, even at very small concentrations. They thus need to be monitored, if not removed or reduced, during physical separation and subsequent hydrometallurgical treatment (Lane et al. 2016; Cook et al. 2018). It is thus essential to obtain a detailed understanding of the mineralogical deportment of ^{226}Ra, ^{210}Pb, and ^{210}Po within the deposit and to qualitatively model the behavior of these RN throughout the processing cycle.

Investigation of uraninite compositions and textures allowed Macmillan et al. (2016) to identify distinct generations of uraninite in the Olympic Dam ore. Although some early uraninite retains the full decay sequence of daughter RN within its crystal structure and may contain >10 wt.% radiogenic Pb, aphanitic uraninite does not and is assumed to have formed much later as a result of the breakdown of

early uraninite or other U-minerals and migration of released U (Xing et al. 2018, 2019). A second study, encompassing brannerite and coffinite in the deposit (Macmillan et al. 2017), shows that these minerals also contain relatively little Pb, strongly supporting the release of U and daughter RN from parent U-minerals and subsequent migration and re-concentration into existing or new minerals.

Rollog et al. (2019) have used nanoSIMS isotope mapping to directly visualize the distribution of ^{226}Ra and ^{210}Pb in representative samples from Olympic Dam. Their results demonstrate decoupling among RN (e.g., ^{226}Ra from ^{238}U) and the migration of daughter RN towards the end of the decay chain at the nm- to μm-scale, formation of new minerals such as galena, and also the concentration of RN at grain boundaries, in microfractures, and trapped in pores within mineral grains. In another copper deposit within the Olympic Cu-Au province, Owen et al. (2018) identified at least two events in which radiogenic lead has been remobilized and separated from parent U and Th and subsequently reconcentrated within nanoscale symplectitic intergrowths of clausthalite (PbSe) within Cu-(Fe)-sulfides. Moreover, the work of Rollog et al. (2019) has suggested that spatial separation of daughter RN from parent U-bearing minerals is accelerated during the final stage of mineral processing, such that recovery of uranium from copper concentrate does not equate to recovery (removal) of ^{226}Ra and ^{210}Pb.

Phosphate minerals are abundant in the Olympic Dam deposit, and include fluorapatite (Krneta et al. 2016, 2017, 2018), florencite-(Ce) and -(La) (Lottermoser 1995; Schmandt et al. 2019a), and subordinate monazite-(Ce) (Lottermoser 1995) and xenotime-(Y) (Oreskes and Einaudi 1990; Ehrig et al. 2012). The deposit also contains wt.% concentrations of baryte (Schmandt et al. 2019b). The latter authors report uptake of Pb, during acid leaching, into baryte that has reported to copper concentrate, highlighting the potential for minor mineral components of the ores or concentrates to act as scavengers of RN.

Collectively, the above studies emphasize the critical importance of careful mineralogical study at appropriate scales of observation to identify RN carriers and assess pathways of RN mobility. Given the potential application of APS minerals in the storage of toxic metals (Kolitsch and Pring 2001), their

widely variable crystal chemistry and low solubilities at high temperature (400-500 °C), and wide ranges of E_h and pH, make them excellent candidates as scavengers of products of radioactive decay.

SAMPLES AND METHODS

Three sets of finely milled samples were collected from the Olympic Dam (OD) processing plant in December 2016: a set of flotation concentrates (FC), a set from the flotation tailings (FT) and a set of concentrates following removal of the majority of uranium via sulfuric acid leaching (Concentrate Leach Discharge, CLD). At Olympic Dam, standard leach conditions are maintained at around 55 °C, pH of 1.5, E_h of ~440 mV (Macnaughton et al. 1999, 2000; Bhargava et al. 2015) for 8-12 hours, depending on the mineralogy of the feed (Ehrig et al. 2015). FC and FT samples have not been chemically altered and are therefore representative of the ore mineralogy whereas CLD samples have become altered during acid leaching. The milled samples were dried and mounted as one-inch polished blocks.

Reflected-light and backscatter-electron (BSE) images were obtained to document textures and compositional zoning using a Nikon Eclipse LV100 POL Petrographic Microscope and an FEI Quanta 450 Field Emission Gun scanning electron microscope equipped with a silicon-drift energy-dispersive X-ray spectrometer (EDS), located at Adelaide Microscopy (The University of Adelaide). Energy-dispersive X-ray spectroscopy (EDS) spot analyses and element maps were collected using an Oxford Instruments Ultim Max 170mm SDD (silicon drift detector) EDS Detector with AZtec software. The SEM was operated in high-vacuum mode at 20 kV and a spot size of 4 μm.

Quantitative compositional data were obtained using a Cameca SX-Five electron probe microanalyzer (EPMA), located at Adelaide Microscopy, and equipped with five tunable wavelength-dispersive spectrometers. The instrument uses PeakSite software for microscope operation, and Probe for EPMA software (distributed by Probe Software Inc.) for data acquisition and processing. Initially, a suite of 40

159 elements (Appendix 1[1]) were analyzed, but after ~40 analyses it was determined that the HREE elements
160 Ho, Yb, Tm, Er, and Dy could be removed from the list to reduce overall count time as they were
161 consistently below, or near below minimum limits of detection (mdl). Due to the measurable amounts of
162 F (and Cl), the halogen oxygen equivalent was subtracted from the stoichiometric oxygen during
163 processing iteration. For major to minor elements, operating conditions were 15 keV and 20 nA Trace
164 element counts were acquired at a higher beam current (100 nA). For all analyses, a spot size of 1 μm
165 was used.

166 Isotope mapping was done with a NanoSIMS 50L (CAMECA, France) at the Centre for Microscopy,
167 Characterization, and Analysis, at the University of Western Australia. A 16 keV primary O^- beam,
168 generated by a Hyperion H200 RF plasma oxygen ion source, was used for all analyses. The instrument
169 was operated in multicollection mode, allowing the simultaneous detection of up to seven isotopes.
170 Positive secondary ion maps were collected for $^{40}Ca^+$, $^{63}Cu^+$, $^{88}Sr^+$, $^{204}Pb^+$, $^{206}Pb^+$, $^{210}RN^+$, $^{226}Ra^+$, $^{230}Th^+$
171 and $^{238}U^+$. To avoid detector saturation, major isotopes of Ca, Sr and U were at times substituted with
172 minor isotopes. Mass calibration was carried out using high-purity metal standards from Astimex. For
173 ^{210}RN and ^{226}Ra, the approximate detector positions were determined from $^{105}Pd_2$ and $^{113}In_2$, respectively.
174 Fine tuning of these detector positions was then carried out on uraninite grains known to contain ^{210}RN
175 and ^{226}Ra. All imaging was done with a 250 pA primary beam, rastering over 50 μm^2 areas (512 px^2),
176 with dwell times of 5.5 ms per pixel; seven planes were recorded for each area. The OpenMIMS plugin
177 (Poczatek et al. 2009) for ImageJ (Schindelin et al. 2012, 2015) was used for all image analysis. All data
178 were dead time corrected and the seven individual planes were aligned before being summed. See Rollog
179 et al. (2019) for discussion on isotope mass interferences.

[1] Deposit item.

This is a preprint, the final version is subject to change, of the American Mineralogist (MSA)
Cite as Authors (Year) Title. American Mineralogist, in press.
DOI: https://doi.org/10.2138/am-2019-7116

180 # RESULTS

181 *Textural Characterization and Mineral Associations*

182 APS phases occur in close association with Cu-Fe-sulfides (bornite and chalcopyrite), hematite, and
183 other more abundant gangue minerals, notably sericitic mica, Fe-dominant chlorites (chamosite),
184 fluorapatite, baryte, and fluorite. Individual APS mineral grains (5-40 μm) show significant contrast
185 variation on BSE images (Fig. 2), consistent with grain-scale compositional zonation. Different zones
186 are variably enriched in REE, Ca, and Sr, whereby brighter zones are typically richer in REE. Several
187 species (REE-, Ca-, and Sr-dominant) are present. BSE imaging and EDS spectra indicate that distinct
188 zones within individual grains also show variation with respect to S and P, suggesting that some are
189 phosphate-dominant, and others are sulfate-dominant. For the purposes of the textural characterization
190 and mineral associations of the APS minerals, there is no discernable difference between samples from
191 floatation and leach processing.

192 APS phases range from range from finely mottled aggregates to elongate needle-like grains (fine
193 plates cut perpendicularly) (Fig. 2a, b respectively), coarsening towards a marked tabular morphology;
194 the latter appearing particularly strongly zoned on backscatter-electron images (Fig. 2c, d). Sr-Ca-
195 dominant APS mineral phases (e.g., svanbergite, woodhouseite) are observed to replace Cu-Fe-sulfides,
196 usually chalcopyrite, often resulting in mutual boundaries with scalloped morphology. Sr-Ca-APS
197 minerals often contain remnants of replaced primary minerals such as the Cu-Fe-sulfides (Fig. 2b) and
198 other gangue minerals including hematite, sericite, and chamosite (Fig. 2a-d). Relics of replaced minerals
199 occur as coarser, island-like inclusions (hematite; Fig. 2a) or speckled inclusion fields within the APS
200 phases (Fig. 2a, c, d).

201 APS minerals are also observed to replace Ca-bearing minerals including fluorapatite (Fig. 3a) and
202 fluorite (Fig. 4a). EDS element maps and corresponding BSE images (Fig. 3b-c) show relics of another
203 Ca-bearing phase partially replaced by APS. Unfortunately, here, the phases measured within the EDS

spectrum, although showing obvious peaks for Ca, Fe, and O, were too mixed to accurately determine the replaced precursor mineral, likely due to their very small grain size and relic nature. Figure 3c shows a Ca-rich zone immediately surrounding partially replaced hematite and associated with Fe-rich chlorite (chamosite), whereas Fig. 3e highlights relics of almost completely replaced fluorapatite inside APS. Some coarser grains (up to 40 μm) of APS phases (Fig. 4a) are characteristically zoned, with the cores recognized as Sr-Ca-dominant and S-bearing (Fig. 4b), through to REE-dominant compositions corresponding to florencite-(Ce) at the rims (Fig. 4c). In contrast to their finer-grained analogues, the coarser-grained APS minerals show negligible replacement of surrounding minerals.

Compositional Data

EPMA data (representative data shown in Tables 1 and 2 and plotted in Figure 5, full dataset in Appendix 2[2]) confirm the presence of two distinct compositional groups indicated by SEM observation (Fig. 4). These plot as distinct clusters but nevertheless form a broad continuum in compositional space (Fig. 5a). With respect to the APS general formula, $AB_3(XO_4)_2(OH)_6$, the two clusters, here defined as Group 1 and Group 2, are discriminated by the dominant A-site cations and the ratios of phosphate to sulfate. Both groups include analyses from FC, FT, and CLD sample types.

Group 1 represents phases with elevated Sr and Ca (Sr>Ca), that are enriched in sulfate (S/(S+P)>0.17) relative to Group 2. Group 1 contains most of the variability within the dataset (Fig. 5). In terms of calculated atom-per-formula-unit (apfu) values, Ca occupancy of the A-site ranges from 0.02 to 0.58, Sr from 0.26 to 0.67, and REE from 0.11 to 0.69. In the X-site, P ranges from 0.81 to 1.55 apfu. S is always subordinate (0.30 to 0.95 apfu). Most analyses within Group 1 thus fall within the compositional field of svanbergite, albeit with strong components of Ca and REE, and with S/(S+P) ratios consistently >0.17 and therefore deviating from ideal stoichiometry. A small number of analyses

[2] Deposit item

included here within Group 1 have REE apfu values that exceed apfu (Sr+Ca). These can be considered as either: (1) Sr-Ca-S-bearing florencite; or (2) mixtures of two or more minerals below the scale of the microprobe beam.

Group 2 phases more closely resemble the composition of florencite-(Ce), i.e., they contain at least 80% occupation of the A site by REE (in order, Ce>La>Nd>Pr). They are also phosphate-dominant, with subordinate sulfate (S/(S+P)<0.17).

Assuming (OH+Cl+F) = 6 apfu, and knowing measured F and Cl concentrations, an estimation of OH occupancy can be made. There appears to be a negative correlation between apfu (Ca+Sr) and calculated OH^-. Also, analyses across both groups containing negligible S tend to have higher calculated OH^- concentrations (Fig. 5b).

Relationships between the dominant A-site cations (Ca, Sr and REE) are compared in ternary diagrams (Fig. 5c, d). An increase in Ca occupancy appears to correlate with increasing Sr content. Analyses close to, or exceeding Sr/(Sr+Ca+REE)>0.5 tend, however, to display much wider variation in Ca content (Fig. 5c). Analytical spots that are richer in REE (~60% or more of A-site occupancy) contain only minimal Ca. Among the REE, either Ce or La is dominant (although La is most often subordinate to Ce) in both Group 1 and 2, and the relative abundance of the remaining REE is low (Fig. 5d). However, as the relative abundance of the remaining REEs (mainly Pr and Nd) increases, there is a marked decrease in La, but a corresponding slight increase in Ce.

Uranium and thorium concentrations are negligible in both groups and rarely above minimum detection limits (mdl). When present, U and Th show only very minor correlation with other elements.

Lead is a trace but nevertheless quantifiable constituent of APS minerals (Tables 1 and 2, Fig. 5e-h). Concentrations are rather variable, however, and correlate with several factors. REE-enriched analyses have low Pb concentrations (<0.006 apfu). Likewise, analytical spots containing elevated P contents were among those with the lowest concentrations of Pb. In contrast, increased Ca and Sr content within the A-

site (Fig. 5e and f, respectively) corresponds with greater Pb content. Pb content also appears to increase with decreasing OH^- and appears in CLD material with greater regularity.

NanoSIMS Isotope Mapping of APS and Associated Minerals

Investigation of selected areas containing APS minerals within the FC and CLD samples by NanoSIMS isotope mapping confirms the presence of ^{226}Ra and ^{210}RN (overwhelmingly ^{210}Pb due to the extreme volatility of ^{210}Po; Rollog et al. 2019) within Sr-Ca-dominant APS minerals (svanbergite). Within most mapped areas such as the examples shown in Figures 6 and 7, there appears to be an excess of daughter ^{226}Ra and ^{210}RN compared to the equivalent map for parent U, which is concentrated within and immediately adjacent to micron-sized U-bearing minerals (in most cases as uraninite). Also, ^{226}Ra and ^{210}RN are seen to be more dispersed throughout the APS minerals relative to U, and the elevated signals for ^{226}Ra and ^{210}RN do not always coincide with those of U. In addition, these radionuclides show greater affinity to APS minerals than either Cu-Fe-sulfide or iron-oxide minerals with only limited dispersion identifiable within the latter. The distribution of ^{210}RN throughout the APS minerals appears to correlate most strongly with that of Ca than the stable product of U decay, ^{206}Pb (Fig. 7). Common Pb represented by ^{204}Pb, however, showed good correlation with ^{210}RN, similarly mimicking Ca composition (Fig. 8). Those domains featuring elevated peak counts for ^{206}Pb lack corresponding peaks on the ^{210}RN map (Fig. 7). This indicates either recent fluid-mediated dispersion of decay products away from the U-bearing minerals and throughout APS, or, alternatively in the case of the CLD samples, interaction with the RN-bearing leach solution and subsequent adsorption. Although these distribution patterns remain qualitative in the absence of suitable standards allowing quantification (Rollog et al. 2019), they nonetheless strongly suggest nanometer- to micron-scale migration of ^{226}Ra and ^{210}RN from parent ^{238}U-bearing phases (either those in the immediate vicinity or possibly migrating from greater distances), and incorporation into APS minerals.

A second significant observation is that Sr-Ca-APS minerals from areas in the CLD samples mapped by nanoSIMS have greater activities of ^{226}Ra and ^{210}RN than their equivalents in the FC samples. This strongly suggests fluid-mineral interaction and, possibly, also sub-solidus diffusion of RN during the leaching process. Observed differences in ^{210}RN concentrations between FC and CLD samples may also be amplified due to the recycling of Cu-sulfate-rich smelter dust (which is consequently enriched in ^{210}RN) into the leach solution to maximize Cu recovery.

DISCUSSION

Composition of APS Minerals

The APS minerals examined by BSE imaging, electron microprobe and nanoSIMS display conspicuous compositional zoning consistent with the formation of an extensive solid solution between end-member APS minerals of the beudantite group. An attempt to use Focused Ion Beam-SEM methods to extract and thin foils for scanning transmission electron microscopy analysis of the APS phases was unsuccessful in that the APS minerals proved too beam-sensitive, even at very low ion beam currents.

Solid solution between svanbergite-woodhouseite and florencite-(REE), (REE)$Al_3(PO_4)_2(OH)_6$, is considered responsible for the measurable concentrations of REE within all analyses. There is complete solid solution between the end-members crandallite, $CaAl_3(PO_4)_2(OH)_6$, and goyazite, $SrAl_3(PO_4)_2(OH)_6$, and between woodhouseite, $CaAl_3(PO_4)(SO_4)(OH)_6$, and svanbergite, $SrAl_3(PO_4)(SO_4)(OH)_6$. We can also assume, that substitution of sulfate for phosphate is continuous (Gaboreau et al. 2007) such that there is solid solution between crandallite-goyazite and woodhouseite-svanbergite series minerals.

The lead concentrations in the analyzed samples are minor but solid solution can be expected to extend to the Pb-bearing analogues of the above minerals, plumbogummite, $PbAl_3(PO_4)_2(OH)_6$, and hinsdalite, $PbAl_3(PO_4)(SO_4)(OH)_6$, with continuous substitution of (Ca,Sr) by Pb. Note that because of its $6s^2$ lone

pair of electrons, Pb causes the reduction of the crystal symmetry in some Pb-rich alunites (Kolitsch and Pring 2001), adding complexity to the Pb substitution.

The measured Pb concentrations may have been incorporated at the time of initial formation of the APS mineral assemblage. Alternatively, Pb may be introduced after crystallization via the following alternative mechanisms. Firstly, released radiogenic Pb may interact with, and be absorbed by, the APS minerals during metamictization of, or diffusion of Pb from adjacent U-bearing minerals such as uraninite, coffinite or brannerite. Secondly, Pb may have migrated in low-temperature hydrothermal fluids and interacted with existing APS minerals during the multiple tectonothermal events over the past ~1.6 Ga, which are interpreted to have impacted on the deposit. Such events are recorded by multiple mineral groups (e.g., Macmillan et al. 2017), and are also recognized from other ore systems in the Olympic Cu-Au Province (Owen et al. 2018). Lastly, acidic fluids containing both Pb and other RN (notably Ra) dissolved in solution may interact with the APS minerals during the acid leach stage of mineral processing, as discussed below.

Aside from the slightly higher Pb concentrations in individual data points from the EPMA dataset (Fig. 5e-h) and the nanoSIMS isotope maps, APS analyzed from CLD material was, for all intents and purposes, identical to that from FC material, indicating negligible modification by the leach liquors. This observation highlights the robust, insoluble character of APS minerals, which remain stable at a broad range of pH and E_h conditions (Kolitsch and Pring 2001).

Radiogenic Pb from decay of U or Th located within the crystal structure of APS minerals is likely very limited. EPMA data (Tables 1 and 2) show only negligible U and Th, barely above mdl in most instances (although detectable with nanoSIMS). NanoSIMS mapping also shows U and Th restricted to inclusions, porous regions within APS or along grain boundaries, even where Pb dispersion is suggested to have taken place (Figs. 6-8). There are currently no APS end-member minerals which contain significant concentrations of uranium (Jambor 1999; Bayliss et al. 2010), whereas a Th-bearing member

of the alunite supergroup, eylettersite [$Th_{0.75}Al_3(PO_4)_2(OH)_6$], is known (Bayliss et al. 2010). Perhaps contrary to this interpretation, Jerden (2007) suggests that U is sequestered by Ba-Sr-Ca-bearing aluminum phosphate minerals of the crandallite group (gorceixite) within an unsaturated soil zone overlying uranium-rich saprolites in the Coles Hill uranium deposit (Virginia). Additionally, electron microprobe compositional data revealing up to 3.44 wt% UO_2 within plumbogummite is presented by Plášil et al. (2009) from supergene altered zones of the Medvědín uranium deposit, Krkonoše Mountains, Czech Republic.

Relationships between the incorporation of Pb and Ca and Sr contents are complex, as evidenced by the EPMA data (Fig. 5e-g) and isotope mapping (Figs. 7 and 8). From the results presented here, we cannot unequivocally state whether Pb is ad- or absorbed by APS grains, however, Schwab et al. (2005) showed that within synthetic crandallite-group phases, thermodynamic stability increases with replacement of Ca^{2+} by Sr^{2+} and Pb^{2+}. The same trend is also recognized in phosphate-sulfate-bearing beudantite-group minerals, albeit to a lesser degree. In any case, the thermodynamic stability increases with replacement in the order of Pb>Sr≥Ca, thus, absorption of Pb by Ca- and Sr-bearing APS grains seems likely. The relatively low thermodynamic stability of Ca^{2+} may be due to its small ionic radii which is suggested to cause contractions within the APS crystal structure resulting in distortions and uneven coordination within the 12-fold coordinated position (Blount 1974). Figure 9 shows the relative positions of the stability fields for each of the woodhouseite series minerals with respect to their dominant A-site cations, with the more stable species plotting closest to the field for gibbsite (Schwab et al. 2005). Studies by Schwab et al. (2004, 2005) show that crandallite and woodhouseite are intimately related and that, in complex natural systems such as Olympic Dam, it is impossible to form pure crandallite without the introduction of substituents such as Sr^{2+} and/or SO_4^{2-}. As such it is unsurprising that we see such a strong association between Ca, Sr and S. This is an important association due to the relative stabilities of each species with respect to variation of pH, and the activities of H_3PO_4 and of HSO_4^- (Fig. 9). In this figure,

344 plumbogummite and hinsdalite are shown to form solid-solutions with their Ca- and Sr-dominant
345 analogues at moderately low pH, with the Pb-bearing phases, particularly hinsdalite, becoming favored
346 as pH and $a\mathrm{HSO_4^-}$ decreases. The phase diagram indicates that there is no point at which single-phase
347 minerals are formed (apart from a small window for hinsdalite at extreme acidity; Fig. 9). Our EPMA
348 data support this in that they show solid-solution members within any given spot, with varying
349 proportions of the end-member components within each analysis (Tables 1 and 2).

350 *Alteration and APS Mineralogy at Olympic Dam*

351 Phosphate minerals are abundant in the Olympic Dam deposit and include fluorapatite (Krneta et al.
352 2016, 2017, 2018), florencite-(Ce) and –(La) (Lottermoser 1995; Schmandt et al. 2019a), and subordinate
353 monazite-(Ce) (Lottermoser 1995) and xenotime-(Y) (Oreskes and Einaudi 1990; Ehrig et al. 2012).
354 Altered mineral assemblages containing APS minerals of the alunite supergroup are interpreted to form
355 via late-stage overprinting during alteration and replacement of paragenetically earlier minerals,
356 observed by the systematic replacement of Cu-(Fe)-sulfides and associated gangue. Several authors (e.g.
357 Bajnóczi et al. 2004; Hikov et al. 2010; Georgieva and Velinova 2012, 2014), report on similar
358 replacement mechanisms within high-sulfidation deposits, occurring during advanced argillic
359 (supergene) alteration. It is noted that while the possibility that an advanced argillic phase taking place
360 at Olympic Dam, represented by the presence of small isolated pockets of remnant sericite + quartz ± Al-
361 OH assemblages, has been discussed previously (Ehrig et al., 2012), there is lack of evidence to suggest
362 that APS is associated with such a phase. Rather, the formation of APS phases is suggested to result from
363 reduced acidic fluids associated with local dissolution of sulfides.

364 Schmandt et al. (2019a) report a similar phase of alteration and replacement of primary mineral
365 assemblages in the Olympic Dam deposit, although focusing on florencite as the dominant REE-
366 phosphate. The mineral associations, textures and LREE trends of the APS minerals discussed here,
367 however, show marked differences to the florencite-dominant compositions presented in Schmandt et al.

(2019a), which were from a suite of drillcore samples anomalously rich in REE. In the present study, based on milled flotation feed and copper concentrates, APS minerals consistently replace Cu-(Fe)-sulfides (almost exclusively chalcopyrite), show distinct zonation with respect to REE, Ca, Sr, S and P, and are variably enriched in Ce over La with increasing Pr and Nd (Fig. 5d). APS mineral textures vary, appearing to depend greatly on the morphology of the original mineral which is being replaced. Coarser grains show excellent zonation in backscatter imaging (Figs. 2c, d and 3), consistently retaining Ca-, Sr-rich cores and REE-rich rims, indicating primary zonation from alkali-earth elements (M^{2+}) to REE (M^{3+}). Replacement of ore minerals formed during the ca. ~1590 Ma onset of mineralization strongly suggests that the APS minerals identified here are paragenetically late. Additionally, the consistent preferential replacement of chalcopyrite over other Cu-(Fe)-sulfides, as confirmed *via* preliminary mineral liberation analysis on materials spanning multiple years of mining activity, suggests some form of association between mineralogical zonation and/or fluid pathways within the deposit and the formation of the APS minerals discussed here. Alternatively, chalcopyrite may simply be more easily replaced by APS minerals than the other Cu-(Fe)-sulfides due to differences in redox potential and pH stability fields.

Florencite-(Ce) in the woodhouseite-svanbergite APS mineral assemblages discussed here fills a gap along a REE mixing trend for minerals previously reported from Olympic Dam (Schmandt et al. 2017). This trend showed a defined separation between La/Ce-enriched florencite and Ce- (and subordinate La-) dominant bastnäsite. The Ce-dominant florencite in the woodhouseite-svanbergite APS mineral assemblages reported on here may therefore represent an intermediary between these two phases. It is suggested that while the Ce- and La-dominant APS mineral assemblages formed broadly simultaneously, migration of REE (likely sourced from pre-existing phosphates), Ca and Sr resulted in the formation of localized 'compositional pockets' of Ce- and La-enriched florencite forming throughout the deposit.

The marked transition of REE-mineral speciation at Olympic Dam, from relatively simple REE-compounds like bastnäsite, through florencite, to the complex solid solutions represented by the alunite-

392 supergroup minerals described here represents an illustrative example of an evolving mineralogical
393 complexity with time, in which successive mineral phases display ever greater structural and chemical
394 complexity (Krivovichev et al. 2018).

395 This compositional variation is likely formed due to differences in thermodynamic stabilities of LREE
396 endmembers, indicated by their Gibbs free energies (Schwab et al. 1993) and by Goldschmidt's rule of
397 ionic radii (Goldschmidt 1937), with thermodynamic stability of $LREEAl_3(PO_4)_2(OH)_6$ endmembers
398 occurring in the order La>Nd>Ce>Sm>Pr>Eu>Gd. As such, the florencite previously reported from
399 Olympic Dam (Schmandt et al. 2019a), in which the La and Ce components are roughly equal, is
400 interpreted to have formed as a combination of direct replacement of pre-existing REE bearing minerals
401 and interaction with an acidic REE-bearing hydrothermal brine (Williams-Jones et al. 2012; Migdisov et
402 al. 2016; Krneta et al. 2018; Schmandt et al. 2019a). Florencite-(Ce) in the APS assemblages reported
403 here is suggested to have formed from a hydrothermal fluid which is either depleted in La or provides
404 the conditions which favored its formation. The conditions at which florencite-(La) forms over florencite-
405 (Ce) are accentuated at low pH with higher pH favoring increased stability of Ce-, Nd-, and Pr-florencite
406 (Schwab et al. 1993). Additionally, Migdisov et al. (2016) have shown that the solubility of Ce, Pr, and
407 Nd increases over that of La with the introduction of sulfate into solution indicating that the dissolution
408 of sulfides (as mentioned above) may also play a key role in the local migration of REE.

409 The dominance of Sr within investigated APS minerals, and the replacement of fluorapatite by
410 svanbergite-dominant APS phases (Fig. 3) adds to evidence for formation from an acidic brine
411 (Stoffregen and Alpers 1987) late in the evolution of the deposit. Additionally, and as discussed by
412 Gaboreau et al. (2007), fluids with a relatively high f_{O_2} favor the incorporation of SO_4 and divalent A-
413 site cations within APS minerals. In reducing environments, sulfur occurs as a reduced species which
414 cannot be incorporated into the APS structure (Gaboreau et al. 2007). Chloride salts are widely regarded
415 as the main transport ligand for metals in hydrothermal fluids, but while $CaCl_2$ and $SrCl_2$ are both

extremely water soluble and likely available, Ca does not readily form crandallite, even in moderately acidic environments (Schwab et al. 2004, 2005). Schwab et al. (2005) have shown that decreasing pH and $a\mathrm{HSO_4^-}$ greatly favor goyazite formation whereas woodhouseite formation is broadly favored by increasing $a\mathrm{HSO_4^-}$ (Fig. 9). Accordingly, we suggest the Sr-dominant phases discussed here formed in a moderately to strongly acidic (micro-)environment with relatively low $a\mathrm{SO_4}$, at least relative to $a\mathrm{PO_4}$.

APS Minerals as RN Scavengers

The EPMA data and nanoSIMS isotope maps represent compelling direct evidence for scavenging of RN (from ^{226}Ra down) by APS minerals, consistent with evidence presented elsewhere, both for products of radioactive decay (Kolitsch and Pring 2001, and references therein) and for removal of toxic metals from mine waste waters such as arsenic and nickel (Monteagudo et al. 2003, 2006). Additionally, within the Oklo uranium deposit (Gabon), Dymkov et al. (1997) identified the migration and incorporation of ^{235}U fission products (Zr and LREE) into Ca-, Sr-, and Ba-bearing APS grains (where Sr and Ba are natural) from adjacent uraninite grains depleted in ^{235}U ($^{235}\mathrm{U}/^{238}\mathrm{U} = 0.0047$). The isotope maps (Figs. 6-8) also indicate that the RN are mobile at the scale of nanometers to microns and become separated from their U-bearing parent phases. Moreover, comparison of isotope maps for FC and CLD samples suggests that scavenging of dissolved RN form as a result of acid leaching is achieved rapidly over the period of hours to days. These observations are critical for understanding the anomalous enrichment in ^{226}Ra and subsequent daughters relative to ^{238}U and ^{232}Th throughout Cu-(U)-ore processing. The inference is clearly that released RN are incorporated into APS phases (as well as baryte; Schmandt et al. 2019b) during the leach process, and also adsorbed onto the surfaces of other minerals, including Cu-(Fe)-sulfides (Rollog et al. 2019). The significance of APS minerals throughout this process lies not only with their observed ability to ad/absorb RN, but also their insolubility, enabling them to survive and possibly even grow during leaching. Although such a statement is difficult to quantify, jarosite ($\mathrm{KFe_3(OH)_6(SO_4)_2}$), a near cousin of APS minerals, is known to form along with gypsum in leach plants,

440 especially in tailings leach where its management can become problematic. There is also potential for
441 formation of new Pb-bearing phases (hinsdalite and/or plumbogummite), or an increase in the hinsdalite
442 and/or plumbogummite components of svanbergite and woodhouseite via replacement of Sr and/or Ca
443 by Pb during acid leaching. Besold et al. (1992) suggest that the Ca^{2+} and Sr^{2+} cations may be replaced
444 within crandallite-group minerals due to the open structure of the alunite-type crystal structure. Such a
445 substitution mechanism is perhaps more viable between Pb and Ca than Pb and Sr and fits well with the
446 models proposed by Schwab et al. (2004, 2005) in which crandallite and woodhouseite stability lessens
447 with decreasing $a HSO_4^-$ at pH ~2-4.

448 Isotope mapping shows that the correlation between ^{210}Pb and ^{206}Pb is relatively weak, particularly in
449 CLD samples, as indicated by the mismatch of 'hot spots' (Fig. 7). At the very least, this suggests distinct
450 mechanisms and pathways for the micron-scale migration of late (i.e. within recent decades) ^{210}Pb
451 throughout the APS minerals compared to the movement and concentration of ^{206}Pb over geological time.
452 ^{210}Pb and ^{204}Pb, however, correlate well, thus indicating the sorption of common Pb via similar
453 mechanisms to that of ^{210}Pb. Whether or not the sorption of common Pb occurred *in situ* or within the
454 processing cycle remains uncertain.

455 ## CONCLUSIONS

456 • Two main compositional groups of APS mineral phases are identified in Olympic Dam ores: one
457 enriched in Sr and/or Ca, and containing SO_4; and the other corresponding to a SO_4-bearing, La-rich
458 Florencite-(Ce). Coarse grains exhibit grain-scale zonation with respect to REE, Ca, Sr, SO_4 and PO_4.
459 • Woodhouseite-svanbergite-dominant APS assemblages are interpreted as paragenetically late with
460 respect to the Cu-(Fe)-sulfides and associated gangue (including hematite, sericite, chamosite and
461 fluorite) which they consistently replace, and also replace earlier REE-bearing phosphates, including
462 fluorapatite, florencite-(La), monazite-(Ce), and xenotime-(Y). This interpretation adds to the
463 growing body of evidence for a hydrothermal overprint at Olympic Dam, probably not exceeding

464 temperatures of 150-200 °C, and represents a valuable contribution to a holistic mineralogical-
465 geochemical-geometallurgical model of REE behavior in the Olympic Dam IOCG-U-Ag deposit.

466 • The APS assemblages appear efficient scavengers of the products of uranium decay. The higher
467 frequency of elevated Pb concentrations recorded in Ca- and Sr-rich zones of APS assemblages, as
468 well as the good overlap on the nanoSIMS isotope maps for Ca and ^{210}Pb, suggest a strong
469 relationship between Ca- and Sr-dominance in APS assemblages and Pb incorporation.

470 • Recorded counts for ^{210}RN are much higher on the nanoSIMS isotope maps of APS minerals from
471 the leach concentrate than the float concentrate, indicating dynamic uptake of ^{210}RN into APS
472 minerals during acid leaching.

473 ## IMPLICATIONS

474 The observed sorption properties of the Ca-Sr-dominant APS minerals and their ability to scavenge
475 RN from the ^{238}U decay chain from ^{226}Ra onwards highlights both the need to suppress natural APS
476 phases in copper concentrates and prevent crystallization of new, anthropogenic APS phases during
477 leaching or elsewhere during the processing-refining cycle. Alternatively, the capacity of APS minerals
478 to scavenge RN could be used in the removal of the products of U decay from processing streams,
479 provided that these phases can be re-dissolved or otherwise removed from the final product.

480 ## ACKNOWLEDGEMENTS

481 This research is a contribution of the ARC Research Hub for Australian Copper-Uranium, co-supported by
482 BHP Olympic Dam, and the South Australian Mining and Petroleum Services Centre of Excellence. Staff at
483 Adelaide Microscopy are acknowledged for assistance with microanalysis as well as referees for providing the
484 knowledge basis for this work. We appreciate the constructive comments from Uwe Kolitsch, Frances Wall, an
485 anonymous reviewer, and Associate Editor Daniel Harlov, which enabled us to clarify the results and
486 interpretations.

REFERENCES

Bayliss, P., Kolitsch, U., Nickel, E.H., and Pring, A. (2010) Alunite supergroup: recommended nomenclature. Mineralogical Magazine, 74, 919–927.

Bajnóczi, B., Seres-Hartai, E., Molnár, F., and Nagy, G. (2004) Phosphate-bearing minerals in the advanced argillic alteration zones of high-sulphidation type ore deposits in the Carpatho-Pannonian region. Acta Mineralogica-Petrographica, Szeged, 45, 81–92.

Besold, E., Bieniek, D., and Kettrup, A. (1992) Synthetischer Crandallit. Umweltwissenschaften und Schadstoff-Forschung, 4(1), 14–16.

Bhargava, S.K., Ram, R., Pownceby, M., Grocott, S., Ring, B., Tardio, J., and Jones, L. (2015) A review of acid leaching of uraninite. Hydrometallurgy, 151, 10–24.

Blount, A.M. (1974). The crystal structure of crandallite. American Mineralogist, 59, 41–47.

Chau, N.D., Jodłowski, P., Kalita, S.J., Olko, P., Chruściel, E., Maksymowicz, A., Waligórski, M.P.R., Bilski, P., and Budzanowski, M. (2008) Natural radiation and its hazard in copper ore mines in Poland. Acta Geophysica, 56, 505–517.

Ciobanu, C.L., Wade, B.P., Cook, N.J., Schmidt Mumm, A., and Giles, D. (2013) Uranium-bearing hematite from the Olympic Dam Cu-U-Au deposit, South Australia: A geochemical tracer and reconnaissance Pb-Pb geochronometer. Precambrian Research, 238, 129–147.

Cook, N.J., Ehrig, K.J., Rollog, M., Ciobanu, C.L., Lane, D.J., Schmandt, D.S., Owen, N.D., Hamilton, T., and Grano, S. (2018) ^{210}Pb and ^{210}Po in geological and related anthropogenic materials: implications for their mineralogical distribution in base metal ores. Minerals, 8, 211

Dymkov, Y., Holliger, P., Pagel, M., Gorshkov, A., and Artyukhina A. (1997) Characterization of a La-Ce-Sr-Ca aluminous hydroxy phosphate in nuclear zone 13 in the Oklo uranium deposit (Gabon). Mineralium Deposita, 32, 617–620.

Ehrig, K., McPhie, J., and Kamenetsky, V.S. (2012) Geology and mineralogical zonation of the Olympic Dam Iron Oxide Cu-U-Au-Ag deposit, South Australia. In: F. Camus, J.W. Hedenquist, M. Harris (eds.), Geology

and Genesis of Major Copper Deposits and Districts of the World, a Tribute to Richard Sillitoe. Society of Economic Geologists Special Publication, 16, 237–267.

Ehrig, K., Liebezeit, V., Macmillan, E., Lower, C., Kamenetsky, V.S., Cook, N.J., and Ciobanu, C.L. (2015) Uranium mineralogy versus the recovery of uranium at Olympic Dam. Proceedings, The AusIMM International Uranium Conference 2015, Adelaide, p. 75.

Gaboreau, S. and Vieillard, P. (2004) Prediction of Gibbs free energies of formation of minerals of the alunite supergroup. Geochimica et Cosmochimica Acta, 68, 3307–3316.

Gaboreau, S., Cuney, M., Quirt, D., Beaufort, D., Patrier, P., and Mathieu, R. (2007) Significance of aluminum phosphate-sulfate minerals associated with U unconformity-type deposits: The Athabasca Basin, Canada. American Mineralogist, 92, 267–280.

Georgieva, S. and Velinova, N. (2012) Alunite from the advanced argillic alterations in the Chelopech high-sulphidation epithermal Cu-Au deposit, Bulgaria: Chemistry, morphology and genetic significance. Geochemistry, Mineralogy and Petrology, 49, 17–31.

Georgieva, S. and Velinova, N. (2014) Florencite-(Ce, La, Nd) and crandallite from the advanced argillic alteration in the Chelopech high-sulphidation epithermal Cu-Au deposit, Bulgaria. Comptes rendus de l'Académie bulgare des sciences: sciences mathématiques et naturelles, 67, 1669–1678.

Goldschmidt, V.M. (1937) The principles of distribution of chemical elements in minerals and rocks. The seventh Hugo Müller Lecture, delivered before the Chemical Society on March 17th, 1937. Journal of the Chemical Society (Resumed), 655–673.

Hikov, A., Lerouge, C., and Velinova, N. (2010) Geochemistry of alunite group minerals in advanced argillic altered rocks from the Asarel porphyry copper deposit, Central Sredno-gorie. Review of the Bulgarian Geological Society 71, 133–148.

Jambor, J.L. (1999) Nomenclature of the alunite supergroup. The Canadian Mineralogist, 37, 1323–1341.

Jerden, J.L. (2007) Uranium sequestration by aluminum phosphate minerals in unsaturated soils. Materials Research Society Symposium Proceedings 985 (Scientific Basis for Nuclear Waste Management XXX), 461–466.

538 Johnson, J.P. and Cross, K.C. (1995) U-Pb geochronological constraints on the genesis of the Olympic Dam Cu-
539 U-Au-Ag deposit, South Australia. Economic Geology, 90, 1046–1063.
540 Kato, T. (1971) The crystal structures of goyazite and woodhouseite. Neues Jahrbuch für Mineralogie
541 Monatshefte, 241–247.
542 Kato, T. and Miura, Y. (1977) The crystal structures of jarosite and svanbergite. Mineralogical Journal, 8(8), 419–
543 430.
544 Kolitsch, U. and Pring, A. (2001) Crystal chemistry of the crandallite, beudantite and alunite groups: a review and
545 evaluation of the suitability as storage materials for toxic metals. Journal of Mineralogical and Petrological
546 Sciences, 96, 67–78.
547 Krneta, S., Ciobanu, C.L., Cook, N.J., Ehrig, K., and Kontonikas-Charos, A. (2016) Apatite at Olympic Dam,
548 South Australia: a petrogenetic tool. Lithos, 262, 470–485.
549 Krneta, S., Ciobanu, C.L., Cook, N.J., Ehrig, K., and Kontonikas-Charos, A. (2017) Rare earth element behaviour
550 in apatite from the Olympic Dam Cu-U-Au-Ag deposit, South Australia. Minerals, 7, 135.
551 Krneta, S., Ciobanu, C.L., Cook, N.J., and Ehrig, K. (2018) Numerical modeling of REE fractionation patterns in
552 fluorapatite from the Olympic Dam deposit (South Australia). Minerals, 8, 342.
553 Krivovichev, S.V., Krivovichev, V.G., and Hazen, R.M. (2018) Structural and chemical complexity of minerals:
554 correlations and time evolution. European Journal of Mineralogy, 30, 231–236.
555 Lane, D.J., Cook, N.J., Grano, S.R., and Ehrig, K. (2016) Selective leaching of penalty elements from copper
556 concentrates: A review. Minerals Engineering, 98, 110–121.
557 Lottermoser, B.G. (1995): Rare earth element mineralogy of the Olympic Dam Cu-U-Au-Ag deposit, Roxby
558 Downs, South Australia; implications for ore genesis. Neues Jahrbuch für Mineralogie, Monatshefte, 1995,
559 371–384.
560 Macmillan, E., Cook, N.J., Ehrig, K., Ciobanu, C.L., and Pring, A. (2016) Uraninite from the Olympic Dam IOCG-
561 U-Ag deposit: linking textural and compositional variation to temporal evolution. American Mineralogist, 101,
562 1295–1320.
563 Macmillan, E., Cook, N.J., Ehrig, K., and Pring, A. (2017) Chemical and textural interpretation of late-stage
564 coffinite and brannerite from the Olympic Dam IOCG-Ag-U deposit. Mineralogical Magazine, 81, 1323–1366.

Macnaughton, S.J., Ring, R.J., Day, A., Collier, D.E., and Tan, L.K.P. (1999) Optimisation of the leach conditions for a copper/uranium ore. In: Mishra, B. (Ed.), Proceedings EPD Congress 1999. The Minerals, Metals and Materials Society, 509–522.

Macnaughton, S.J., Tan, L., Day, A., and Ring, R.J. (2000) Modelling the leaching behaviour of an uranium ore. In: Uranium 2000: International Symposium on the Process Metallurgy of Uranium, Saskatoon, SK, 413–427

Migdisov, A., Williams-Jones, A.E., Brugger, J., and Caporuscio, F.A. (2016) Hydrothermal transport, deposition, and fractionation of the REE: Experimental data and thermodynamic calculations. Chemical Geology, 439, 13–42.

Monteagudo, J.M., Durán, A., Carmona, M.S., Schwab, R.G., and Higueras, P. (2003) Elimination of inorganic mercury from waste waters using crandallite-type compounds. Journal of Chemical Technology and Biotechnology, 78, 399–405.

Monteagudo, J.M., Durán, A., Martín, I.S., and Schwab, R.G. (2006) Treatment of aqueous solutions containing nickel using crandallite-type compounds. Journal of Chemical Technology and Biotechnology, 81, 262–267.

Oreskes, N. and Einaudi, M.T. (1990). Origin of rare earth element-enriched hematite breccias at the Olympic Dam Cu-U-Au-Ag deposit, Roxby Downs, South Australia. Economic Geology, 85(1), 1–28.

Owen, N.D., Ciobanu, C.L., Cook, N.J., Slattery, A., and Basak, A. (2018) Nanoscale study of clausthalite-bearing symplectites in Cu-Au-(U) ores: Implications for ore genesis. Minerals, 8(2), 67; doi:10.3390/min8020067.

Pe-Piper, G. and Dolansky, L.M. (2005) Early diagenetic origin of Al phosphate-sulfate minerals (woodhouseite and crandallite series) in terrestrial sandstones, Nova Scotia, Canada. American Mineralogist, 90, 1434–1441.

Plášil, J., Sejkora, J., Čejka, J., Škoda, R., and Goliáš, V. (2009): Supergene mineralization of the Medvědín uranium deposit, Krkonoše Mountains, Czech Republic. Journal of Geosciences, 54, 15–56.

Poczatek, C., Kaufman, Z., and Lechene, C. (2009) OpenMIMS ImageJ Plugin Guide. Harvard Medical School, Boston, Massachusetts, USA.

Rasmussen, B. (1996) Early-diagenetic REE-phosphate minerals (florencite, gorceixite, crandallite, and xenotime) in marine sandstones; a major sink for oceanic phosphorus. American Journal of Science, 296, 601–632.

590 Rollog, M., Cook, N.J., Gugliardo, P., Ehrig. K., and Kilburn, M. (2019) In situ spatial distribution mapping of
591 radionuclides in minerals by nanoSIMS. Geochemistry – Exploration, Environment, Analysis;
592 https://doi.org/10.1144/geochem2018-038
593 Schindelin, J., Arganda-Carreras, I., Frise, E., Kaynig, V., Longair, M., Pietzsch, T., Preibisch, S., Rueden, C.,
594 Saalfeld, S., Schmid, B., and Tinevez, J.Y. (2012) Fiji: an open-source platform for biological-image analysis.
595 Nature Methods, 9, 676–682.
596 Schindelin, J., Rueden, C.T., Hiner, M.C., and Eliceiri, K.W. (2015) The 516 ImageJ ecosystem: An open platform
597 for biomedical image analysis. Molecular Reproduction and Development, 82, 518–529.
598 Schmandt, D.S., Cook, N.J., Ehrig, K., Ciobanu, C.L., Wade, B.P., Gilbert, S., and Kamenetsky, V.S. (2017) Rare
599 earth element fluorocarbonate minerals from the Olympic Dam Cu-U-Au-Ag deposit, South Australia.
600 Minerals, 7, 202.
601 Schmandt, D.S., Cook, N.J., Ciobanu, C.L., Ehrig, K., Wade, B.P., Gilbert, S., and Kamenetsky, V.S. (2019a).
602 Rare earth element phosphate minerals from the Olympic Dam Cu-U-Au-Ag deposit, South Australia:
603 Recognizing temporal-spatial Controls on REE mineralogy in an evolved IOCG system. The Canadian
604 Mineralogist, 57, 3–24.
605 Schmandt, D.S., Cook, N.J., Ehrig, K., Gilbert, S., Wade, B.P., Rollog, M., Ciobanu, C.L., and Kamenetsky, V. S.
606 (2019b). Uptake of trace elements by baryte during copper ore processing: A case study from Olympic Dam,
607 South Australia. Minerals Engineering, 135, 83–94.
608 Schwab, R.G., Götz, C., Herold, H., and Pinto de Oliveira, N. (1993) Compounds of the crandallite type:
609 thermodynamic properties of Ca-, Sr-, Ba-, Pb-, La-, Ce-to Gd-phosphates and -arsenates. Neues Jahrbuch für
610 Mineralogie Monatshefte, 551–568.
611 Schwab, R.G., Pimpl, T., Schukow, H., Stolle, A., and Breitinger, D.K. (2004) Compounds of the crandallite-type:
612 Synthesis, properties and thermodynamic data of pure crandallite and woodhouseite. Neues Jahrbuch für
613 Mineralogie Monatshefte, 385–409.
614 Schwab, R.G., Pimpl, T., Schukow, H., Stolle, A., and Breitinger, D.K. (2005) Compounds of the crandallite-type:
615 Synthesis, properties and thermodynamic data of Ca–Sr–Ba–Pb-(arseno)-woodhouseites. Neues Jahrbuch für
616 Mineralogie Abhandlungen, 181, 207–218.

Stoffregen, R.E. and Alpers, C.N. (1987) Woodhouseite and svanbergite in hydrothermal ore deposits; products of apatite destruction during advanced argillic alteration. The Canadian Mineralogist, 25, 201–211.

Triplehorn, D.M., Stanton, R.W., Ruppert, L.F., and Crowley, S.S. (1991) Volcanic ash dispersed in the Wyodak-Anderson coal bed, Powder River basin, Wyoming. Organic Geochemistry, 17, 567–575.

Verdugo-Ihl, M.R., Ciobanu, C.L., Cook, N.J., Ehrig, K., Courtney-Davies, L., and Gilbert, S. (2017) Textures and U-W-Sn-Mo signatures in hematite from the Cu-U-Au-Ag orebody at Olympic Dam, South Australia: defining the archetype for IOCG deposits. Ore Geology Reviews, 91, 173–195.

Williams-Jones, A.E., Migdisov, A.A., and Samson, I.M. (2012). Hydrothermal mobilisation of the rare earth elements–a tale of "ceria" and "yttria". Elements, 8, 355–360.

Xing, Y., Mei, Y., Etschmann, B., Liu, W., and Brugger, J. (2018) Uranium transport in F-Cl-bearing fluids and hydrothermal upgrading of U-Cu ores in IOCG deposits. Geofluids (special issue), 2018, Article ID 6835346, 22 pages.

Xing, Y., Etschmann, B., Liu, W., Mei, Y., Shvarov, Y., Testemale, D., Tomkins, A. and Brugger, J. (2019) The role of fluorine in hydrothermal mobilization and transportation of Fe, U and REE and the formation of IOCG deposits. Chemical Geology, 504, 158–176.

Zema, M., Callegari, A.M., Tarantino, S.C., Gasparini, E., and Ghigna, P. (2012) Thermal expansion of alunite up to dehydroxylation and collapse of the crystal structure. Mineralogical Magazine, 76, 613–623.

Figure captions

Figure 1: The crystal structure of APS minerals looking down the [001] zone axis (left) and just offset from [110] (right). Red atoms: A-site cations; blue atoms: Al; yellow atoms: P/S; black atoms: OH/H_2O; grey atoms: O. Note 12-fold coordination of A-site cations, electrostatically and H-bonded to OH, H_2O and O within AlO_6 octahedra and phosphate/sulfate tetrahedra. Data from Kato (1971).

Figure 2: BSE images of APS and associated minerals. Images (**a**-**d**) are arranged in order of APS grain coarsening; (**a**) shows one of the finest-scale grained morphologies of the APS minerals observed. Note the mottled appearance of the aggregate relative to the coarser, clean surface of APS next to the replacement zones around hematite (Hm); (**b**), (**c**) and (**d**) show the formation of needles (coarser in **c** and **d**) of APS as the APS replaces

sericite (Ser) and chlorite (chamosite) (Chl), hematite and chalcopyrite (Cp). Relic replaced hematite and chalcopyrite are preserved within the APS grains (**c** and **d**) as indicated by the light speckling. More platy, tabular APS crystals are formed in (**c**) replacing chlorite (chamosite) (Chl) and bornite (Bn). Note that with coarsening of the APS minerals, zonation becomes more evident (**c** and **d**). Images (**a**), (**c**) and (**d**) are taken from FC material, (**b**) is taken from CLD material.

Figure 3: BSE images showing (a) replacement of Ca-bearing minerals such as fluorapatite (Ap) by APS phases, as well as chlorite (chamosite) (Chl) (**a**) and (**b**). Cu-(Fe)-sulfides chalcopyrite (Cp) and bornite (Bn) are also replaced by APS in (**b**) and (**d**), respectively. Images (**c**) and (**e**) are X-ray element distribution maps taken from the areas identified by the boxes in (**b**) and (**d**) and show the presence of remnant Ca-bearing phases encased within APS. S = red, Fe = purple, Al = blue, and Ca = yellow. All imaged grains are from FC material.

Figure 4: (**a**) BSE image of subhedral tabular APS crystals in association with fluorite (Ft), hematite (Hm) and chalcopyrite (Cp). (**b**) and (**c**) show EDS spectra obtained from locations marked on (**a**). Brighter zones on APS grains resemble florencite in composition, whereas the darker zones contain Sr, Ca and S. Image taken from FC material.

Figure 5: EPMA compositional data (apfu from formulae) for APS minerals plotted in terms of (**a**) (Ca+Sr)/(Ca+Sr+REE) vs. S/(S+P). Two groups are discriminated by the two variables. (**b**) S/(S+P) vs. (Ca+Sr)/OH^-; (**c**-**d**) Ternary plots illustrating the relative abundances of A-site cations in terms of (**c**) Ca-Sr-REE and (**d**) La–Ce–[REE-(La+Ce)] where the major component of [REE-(La+Ce)] is (Pr+Nd); (**e, f)** show Pb (apfu) as a function of (Ca+Sr)/(Ca+Sr+REE) and S/(S+P), respectively; (**g**) and (**h**) show Pb/REE as a function of Ca/P and Sr/P, respectively. Note that values below mdl are not shown, resulting in fewer points on some plots. The dark grey dots mark the positions of the endmember compositions as indicated. FC and CLD material is shown by the empty and filled dots respectively.

Figure 6: BSE image (left) of a grain from FC, with nanoSIMS maps for ^{234}U, ^{230}Th, ^{226}Ra and ^{210}RN as overlays (see annotations). APS minerals replace chalcopyrite (Cp) and hematite (Hm). Uraninite (Un) inclusions are indicated along grain boundaries and within APS. Note the concentration of ^{234}U counts towards the bottom left side of the image (indicated by the white arrow) does not correspond to a comparable feature on the ^{226}Ra map. Note also that ^{210}RN appear restricted to the U-bearing inclusions and APS minerals only.

Figure 7: BSE image of a grain from CLD sample with nanoSIMS maps of ^{238}U, ^{226}Ra, ^{210}RN, ^{206}Pb and ^{40}Ca as overlays (see annotations). Chalcopyrite (Cp) is undergoing replacement by APS, with grains of uraninite (Un) occurring within chalcopyrite. ^{238}U is restricted to uraninite and porous regions in APS whereas RN become progressively more dispersed within the APS (^{226}Ra mostly overlying zones with concentrated ^{238}U counts, ^{210}RN throughout). The correspondence between 'hot spots' of ^{210}RN and ^{206}Pb is relatively moderate, possibly indicating complex micron-scale migration of RN and/or stable radiogenic Pb. Note, however, the excellent correlation between ^{210}RN and ^{40}Ca. Also note the three spots vacant of counts in the central region of the ^{206}Pb and ^{40}Ca maps, likely resulting from the presence of sub-surface sericite within the analysis.

Figure 8: BSE image of a grain from CLD sample with nanoSIMS maps of ^{238}U, ^{226}Ra, ^{210}RN, ^{204}Pb and ^{40}Ca as overlays (see annotations). APS replaces sericite (Ser), hematite (Hm) and chalcopyrite (Cp). Note the prevalence of U along grain boundaries between APS and hematite, and hematite and sericite. Both ^{210}RN and ^{204}Pb match well with ^{40}Ca.

Figure 9: Garrel phase diagram of the system $MO\text{-}Al_2O_3\text{-}P_2O_5\text{-}SO_3\text{-}H_2O$ at 333K. $[H_3PO_4] = 10^{-5.2}$ mol.L^{-1}, $[M^{2+}]=[Al^{3+}] = 10^{-3}$ mol.L^{-1}. $M^{2+} = Ca^{2+}$, Sr^{2+}, or Pb^{2+}, Crnd = crandallite, positions of gibbsite ($Al(OH)_3$), augelite ($Al_2(PO_4)(OH)_3$), and hydroxylapatite ($Ca_5(PO_4)_3(OH)$) are shown. Modified after Schwab et al. (2005).

Table 1: Representative EPMA data for APS minerals of Group 1 based on the ideal formula $AB_3(XO_4)_2(OH)_6.nH_2O$.

					Oxides (wt%)					
Material	**CLD**	**CLD**	**FC**	**FC**	**CLD**	**FC**	**FC**	**FC**	**FC**	**FC**
Na_2O	0.035	<mdl	0.049	0.072	0.114	0.119	0.129	0.064	0.125	0.081
K_2O	0.189	0.018	0.134	0.085	0.169	0.340	0.303	0.362	0.340	0.274
CaO	0.26	0.26	1.29	1.60	2.54	3.16	2.20	2.37	2.37	2.80
SrO	5.10	5.79	9.58	10.60	10.80	11.23	13.86	13.42	14.22	13.32
BaO	0.160	0.101	0.420	0.508	0.522	0.412	0.477	0.363	0.578	0.296
Y_2O_3	0.033	<mdl	0.230	0.377	0.192	0.037	0.154	0.047	0.132	0.027
ZrO_2	0.063	0.069	0.052	0.058	0.071	0.073	0.066	0.075	0.070	0.055
La_2O_3	7.48	7.04	3.94	4.10	2.76	1.65	1.50	1.34	1.33	1.16
Ce_2O_3	10.64	11.10	8.35	6.48	5.97	3.24	2.44	2.22	2.24	2.07
Pr_2O_3	0.89	0.86	0.87	0.64	0.62	0.43	0.16	0.26	0.23	0.10
Nd_2O_3	1.94	2.17	1.83	1.11	1.70	1.12	0.69	0.55	0.58	0.53
Sm_2O_3	<mdl	0.088	0.203	0.174	0.169	0.136	0.065	<mdl	<mdl	<mdl
Eu_2O_3	0.046	0.087	0.055	0.059	0.078	0.138	<mdl	<mdl	<mdl	<mdl
Gd_2O_3	<mdl	<mdl	<mdl	<mdl	0.104	0.082	<mdl	<mdl	<mdl	0.114
Tb_2O_3	<mdl	<mdl	0.065	0.066	0.042	0.000	<mdl	<mdl	<mdl	<mdl
Dy_2O_3	<mdl	<mdl				0.062				
Bi_2O_3	<mdl	<mdl	0.092	<mdl	<mdl	0.032	<mdl	<mdl	<mdl	<mdl
PbO	<mdl	<mdl	<mdl	<mdl	0.250	0.315	0.233	0.454	0.292	0.270
ThO_2	0.000	0.203	<mdl	<mdl	<mdl	<mdl	0.027	<mdl	<mdl	0.031
UO_2	0.022	0.022	<mdl	0.027	0.023	0.024	0.019	0.021	<mdl	<mdl
MgO	<mdl	<mdl	0.026	0.012	0.029	0.027	0.067	0.040	0.018	0.016
Al_2O_3	32.89	31.69	34.87	32.56	35.83	36.20	34.33	35.40	36.25	36.16
TiO_2	0.032	0.077	0.016	0.033	0.025	0.021	<mdl	0.018	<mdl	0.015
Fe_2O_3	3.28	1.86	1.44	2.18	0.89	1.55	1.27	0.90	0.84	1.28
Cu_2O	0.693	0.811	0.626	0.320	0.971	0.385	0.524	0.510	0.638	0.589
Nb_2O_5	0.026	<mdl	<mdl	0.026	<mdl	<mdl	0.023	<mdl	0.035	<mdl
Ta_2O_5	0.107	0.073	<mdl	<mdl	<mdl	<mdl	<mdl	<mdl	0.047	<mdl
WO_3	0.109	<mdl	<mdl	0.071	<mdl	0.086	<mdl	<mdl	<mdl	<mdl
SiO_2	0.803	0.299	0.933	0.499	0.271	0.967	0.227	0.609	0.176	0.322
P_2O_5	19.17	19.25	19.96	20.61	18.01	19.79	22.13	20.78	22.02	20.06
SO_3	3.73	4.14	3.75	3.90	6.54	8.60	5.75	9.23	6.56	9.55
As_2O_3	0.070	<mdl	<mdl	<mdl	<mdl	<mdl	<mdl	<mdl	<mdl	<mdl
F	0.119	0.395	2.065	3.051	2.624	1.451	3.432	1.995	3.042	1.277
Cl	0.025	0.000	0.030	0.000	0.041	0.031	0.000	0.038	0.016	0.021
Total	**87.92**	**86.39**	**90.89**	**89.21**	**91.36**	**91.73**	**90.08**	**91.06**	**92.15**	**90.41**
					APS Formula (apfu)					
					A-Site					
Na	0.006	0.000	0.008	0.012	0.018	0.018	0.020	0.010	0.019	0.012
K	0.021	0.002	0.014	0.009	0.018	0.034	0.032	0.036	0.034	0.027
Ca	0.024	0.025	0.116	0.148	0.228	0.265	0.193	0.200	0.201	0.235
Sr	0.257	0.299	0.468	0.529	0.523	0.511	0.658	0.612	0.654	0.607
Ba	0.005	0.004	0.014	0.017	0.017	0.013	0.015	0.011	0.018	0.009
Y	0.002	-	0.010	0.017	0.009	0.002	0.007	0.002	0.006	0.001
Zr	0.003	0.003	0.002	0.002	0.003	0.003	0.003	0.003	0.003	0.002
La	0.239	0.232	0.122	0.130	0.085	0.048	0.045	0.039	0.039	0.034
Ce	0.338	0.363	0.258	0.204	0.183	0.093	0.073	0.064	0.065	0.059
Pr	0.028	0.028	0.027	0.020	0.019	0.012	0.005	0.007	0.007	0.003
Nd	0.060	0.069	0.055	0.034	0.051	0.031	0.020	0.015	0.016	0.015
Sm	-	0.003	0.006	0.005	0.005	0.004	0.002	-	-	-
Eu	0.001	0.003	0.002	0.002	0.002	0.004	-	-	-	-
Gd	-	-	-	-	0.003	0.002	-	-	-	0.003

Tb	-	-	0.002	0.002	0.001	-	-	-	-	-
Dy	-	-				0.002				
Total REE	**0.67**	**0.70**	**0.47**	**0.40**	**0.35**	**0.20**	**0.14**	**0.13**	**0.13**	**0.11**
Bi	0.004	0.003	-	-	-	-	-	-	0.002	-
Pb	-	-	-	-	0.006	0.007	0.005	0.010	0.006	0.006
Th	-	0.004	-	-	-	-	-	-	-	0.001
U	-	-	-	0.001	-	-	-	-	-	-
Total	**1.66**	**1.73**	**1.57**	**1.53**	**1.52**	**1.24**	**1.22**	**1.14**	**1.20**	**1.13**
					B-Site					
Mg	-	-	0.003	0.002	0.004	0.003	0.008	0.005	0.002	0.002
Al	3.37	3.33	3.46	3.31	3.53	3.34	3.31	3.28	3.39	3.35
Mn	-	-	-	-	-	-	-	-	0.003	-
Fe	0.32	0.19	0.14	0.21	0.08	0.14	0.12	0.08	0.07	0.11
Cu	0.045	0.055	0.040	0.021	0.061	0.023	0.032	0.030	0.038	0.035
Nb	0.001	-	-	0.001	-	-	0.001	-	0.001	-
Ta	-	-	0.001	-	-	-	-	-	-	-
W	0.002	-	-	0.002	-	0.002	-	-	-	-
Ti	0.002	0.005	0.001	0.002	0.002	0.001	-	0.001	-	0.001
Total	**3.74**	**3.58**	**3.64**	**3.55**	**3.68**	**3.51**	**3.47**	**3.40**	**3.51**	**3.50**
					X-Site					
Si	0.070	0.027	0.079	0.043	0.023	0.076	0.019	0.048	0.014	0.025
P	1.41	1.45	1.42	1.50	1.27	1.31	1.53	1.38	1.48	1.33
S	0.30	0.35	0.30	0.31	0.51	0.63	0.44	0.68	0.49	0.70
Total	**1.78**	**1.83**	**1.80**	**1.86**	**1.81**	**2.02**	**1.99**	**2.11**	**1.98**	**2.06**
					Anions					
O	8	8	8	8	8	8	8	8	8	8
F	0.033	0.112	0.550	0.831	0.693	0.360	0.889	0.497	0.763	0.317
Cl	0.004	-	0.004	-	0.006	0.004	-	0.005	0.002	0.003
OH	**5.96**	**5.89**	**5.45**	**5.17**	**5.30**	**5.64**	**5.11**	**5.50**	**5.23**	**5.68**

Notes: mdl: minimum limit of detection; Components that were consistently below minimum detection limit (mdl) values are not given. Blank spaces indicate that no measurement was taken for the given element in that analysis (see text).

Table 2: Representative EPMA data for APS minerals of Group 2 based on the ideal formula $AB_3(XO_4)_2(OH)_6.nH_2O$.

					Oxides (wt%)					
Material	**FT**	**FT**	**FT**	**FC**	**FC**	**FT**	**CLD**	**CLD**	**CLD**	**CLD**
Na_2O	<mdl	<mdl	<mdl	<mdl	<mdl	0.035	<mdl	<mdl	<mdl	<mdl
K_2O	0.024	0.192	0.014	0.012	0.009	0.063	0.009	<mdl	<mdl	0.018
CaO	0.38	0.15	0.20	0.20	0.28	0.33	0.28	0.26	0.28	0.54
SrO	1.61	1.48	2.15	2.38	2.19	2.28	2.24	2.53	2.53	2.58
BaO					0.096		0.062	0.196	0.493	0.155
Y_2O_3	0.021	0.023	0.055	0.044	<mdl	0.051	<mdl	0.022	0.040	0.092
ZrO_2	<mdl	<mdl	<mdl	<mdl	0.034	<mdl	0.040	0.028	0.057	0.054
La_2O_3	8.97	8.72	6.73	9.43	11.23	13.64	7.82	11.09	11.21	9.41
Ce_2O_3	15.72	13.95	14.26	14.59	13.41	12.93	11.68	12.87	12.68	13.74
Pr_2O_3	1.38	1.26	1.47	1.03	0.70	0.60	0.90	0.67	0.76	1.07
Nd_2O_3	3.57	3.08	4.69	2.24	1.11	0.98	2.58	1.18	1.09	1.96
Sm_2O_3	0.212	0.122	0.357	<mdl	0.075	<mdl	0.189	0.082	<mdl	<mdl
Eu_2O_3	0.046	0.038	0.086	<mdl	<mdl	<mdl	<mdl	<mdl	0.041	<mdl
Tb_2O_3	<mdl	<mdl	<mdl	<mdl	<mdl	<mdl	<mdl	<mdl	0.048	<mdl
Dy_2O_3	<mdl	<mdl	<mdl	<mdl	<mdl	<mdl	<mdl	<mdl	<mdl	0.055
Ho_2O_3	<mdl	<mdl	<mdl	<mdl	<mdl	<mdl	<mdl	0.203	<mdl	<mdl
Yb_2O_3	<mdl	<mdl	<mdl	<mdl	<mdl	0.327	<mdl	<mdl	<mdl	<mdl
Bi_2O_3					<mdl		<mdl	<mdl	0.032	<mdl
PbO	<mdl	<mdl	0.027	<mdl	<mdl	<mdl	<mdl	0.184	0.145	0.245
ThO_2	<mdl	0.061	0.020	<mdl	<mdl	<mdl	<mdl	<mdl	<mdl	<mdl
UO_2	<mdl	<mdl	<mdl	<mdl	0.019	<mdl	0.041	<mdl	<mdl	0.037
MgO					<mdl		0.015	<mdl	<mdl	0.035
Al_2O_3	29.77	28.88	28.86	29.78	32.55	30.40	29.36	31.72	31.74	32.23
TiO_2					<mdl		<mdl	<mdl	0.036	0.045
Fe_2O_3	1.33	0.68	3.30	3.15	0.73	2.63	9.64	0.76	0.65	1.09
Cu_2O					0.710		0.942	0.687	0.593	0.648
Nb_2O_5	<mdl	<mdl	<mdl	<mdl	<mdl	<mdl	0.023	0.028	<mdl	<mdl
Ta_2O_5					<mdl		<mdl	0.089	<mdl	<mdl
WO_3					0.000		<mdl	<mdl	0.115	<mdl
SiO_2	<mdl	<mdl	<mdl	<mdl	0.399	<mdl	0.718	0.306	0.341	0.460
P_2O_5	19.75	20.42	19.50	17.26	19.55	19.29	18.75	19.98	20.08	19.57
SO_3	0.72	0.77	0.67	1.49	1.83	1.56	1.42	2.00	2.09	1.54
As_2O_3	<mdl	<mdl	0.688	0.156	0.293	0.031	<mdl	0.280	0.225	0.030
F	0.265	0.064	0.061	0.218	0.235	0.219	<mdl	0.224	0.208	0.335
Cl	0.031	0.097	0.035	0.073	0.025	0.030	0.031	0.024	0.027	0.056
Total	**83.80**	**79.99**	**83.18**	**82.06**	**85.49**	**85.41**	**86.75**	**85.42**	**85.51**	**86.00**
					APS Formula (apfu)					
					A-Site					
Na	-	-	-	-	-	0.006	-	-	-	-
K	0.003	0.024	0.002	0.001	0.001	0.007	0.001	-	-	0.002
Ca	0.04	0.02	0.02	0.02	0.03	0.03	0.03	0.03	0.03	0.05
Sr	0.09	0.08	0.12	0.14	0.12	0.12	0.12	0.13	0.13	0.14
Ba					0.003		0.002	0.007	0.018	0.006
Y	0.001	0.001	0.003	0.002	-	0.003	-	0.001	0.002	0.004
Zr	-	-	-	-	0.001	-	0.002	0.001	0.003	0.002
La	0.32	0.31	0.24	0.34	0.38	0.47	0.26	0.37	0.38	0.32
Ce	0.55	0.50	0.50	0.52	0.45	0.44	0.39	0.43	0.42	0.46
Pr	0.05	0.04	0.05	0.04	0.02	0.02	0.03	0.02	0.03	0.04
Nd	0.12	0.11	0.16	0.08	0.04	0.03	0.08	0.04	0.04	0.06
Sm	0.007	0.004	0.012	-	0.002	-	0.006	0.003	-	-
Eu	0.002	0.001	0.003	-	-	-	-	-	0.001	-

Tb	-	-	-	-	-	-	-	-	0.001	-
Ho	-	-	-	-	-	-	-	0.006	-	-
Yb	-	-	-	-	-	0.009	-	-	-	-
Total REE	**1.04**	**0.97**	**0.97**	**0.98**	**0.89**	**0.97**	**0.77**	**0.87**	**0.86**	**0.87**
Bi					-		-	0.004	-	-
Pb	-	-	0.001	-	-	-	-	0.005	0.004	0.006
Th	0.000	0.001	-	-	-	-	-	-	-	-
U	-	-	-	-	0.000	-	0.001	-	-	0.001
Total	**1.18**	**1.10**	**1.11**	**1.14**	**1.04**	**1.15**	**0.92**	**1.05**	**1.05**	**1.09**
					B-Site					
Mg					-		0.002	-	-	0.005
Al	3.35	3.33	3.27	3.44	3.49	3.34	3.14	3.41	3.41	3.46
Fe	0.144	0.075	0.358	0.348	0.075	0.277	0.986	0.078	0.066	0.112
Cu					0.049		0.064	0.047	0.041	0.045
Nb	-	-	-	-	-	-	0.001	0.001	-	-
W					-		-	-	0.003	-
Ti					-		-	-	0.002	0.003
Total	**3.50**	**3.40**	**3.63**	**3.79**	**3.62**	**3.62**	**4.19**	**3.54**	**3.52**	**3.63**
					X-Site					
Si	-	-	-	-	0.036	-	0.065	0.028	0.031	0.042
P	1.60	1.69	1.59	1.43	1.51	1.52	1.44	1.54	1.55	1.51
S	0.06	0.07	0.06	0.14	0.16	0.14	0.12	0.17	0.18	0.13
As	-	-	0.040	0.009	0.016	0.002	-	0.016	0.012	0.002
Total	**1.66**	**1.76**	**1.69**	**1.58**	**1.72**	**1.66**	**1.62**	**1.76**	**1.77**	**1.69**
					Anions					
O	8.000	8.000	8.000	8.000	8.000	8.000	8.000	8.000	8.000	8.000
F	0.080	0.020	0.019	0.068	0.068	0.065	-	0.065	0.060	0.097
Cl	0.005	0.016	0.006	0.012	0.004	0.005	0.005	0.004	0.004	0.009
OH	**5.91**	**5.96**	**5.98**	**5.92**	**5.93**	**5.93**	**6.00**	**5.93**	**5.94**	**5.89**

Notes: mdl: minimum limit of detection; Components that were consistently below minimum detection limit (mdl) values are not given. Blank spaces indicate that no measurement was taken for the given element in that analysis (see text).

Figure 1

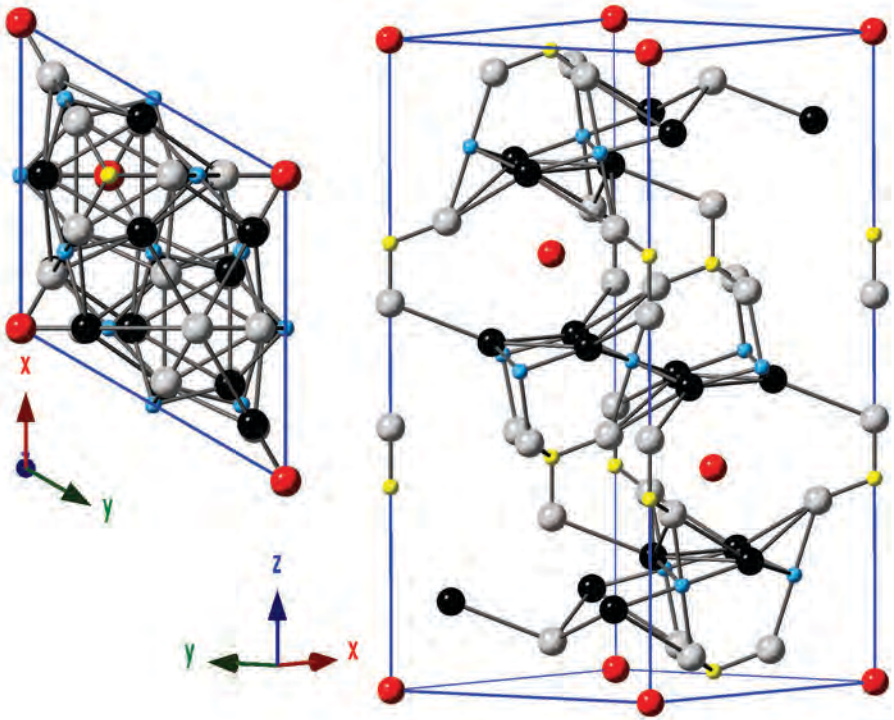

Figure 2

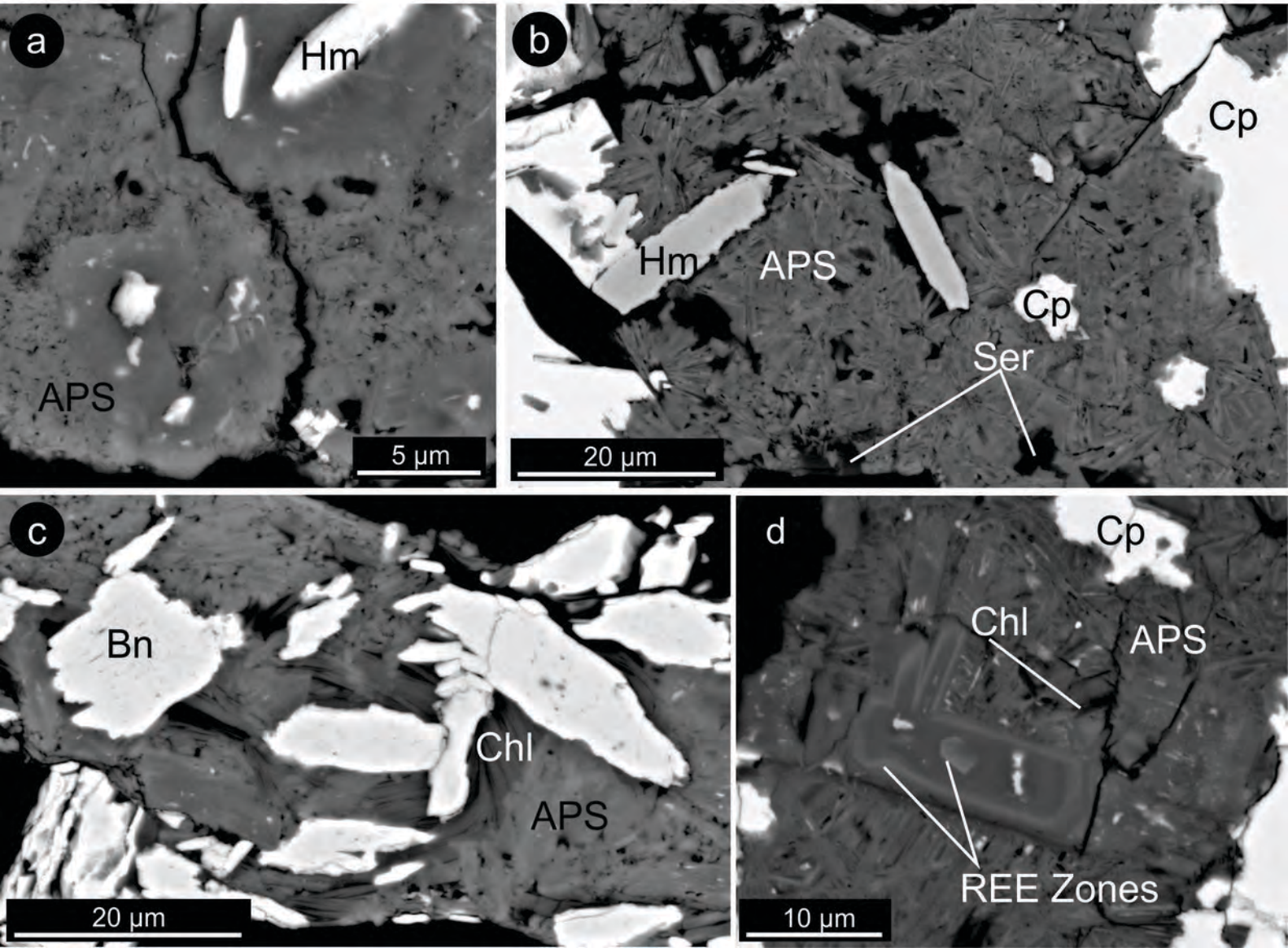
a
Hm
APS
5 µm
b
Cp
Hm
APS
Cp
Ser
20 µm
c
Bn
Chl
APS
20 µm
d
Cp
Chl
APS
REE Zones
10 µm

Figure 3

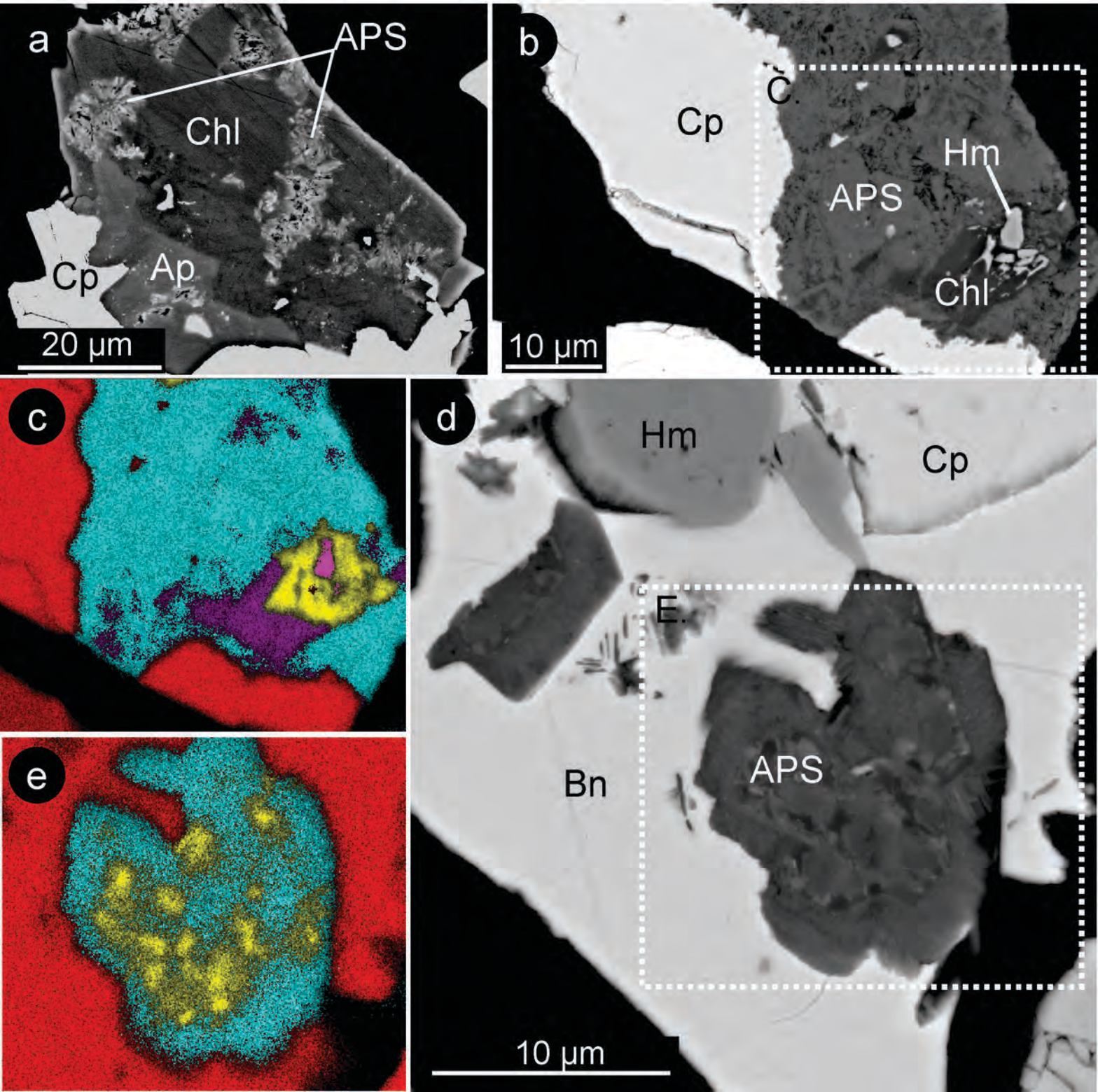

Figure 4

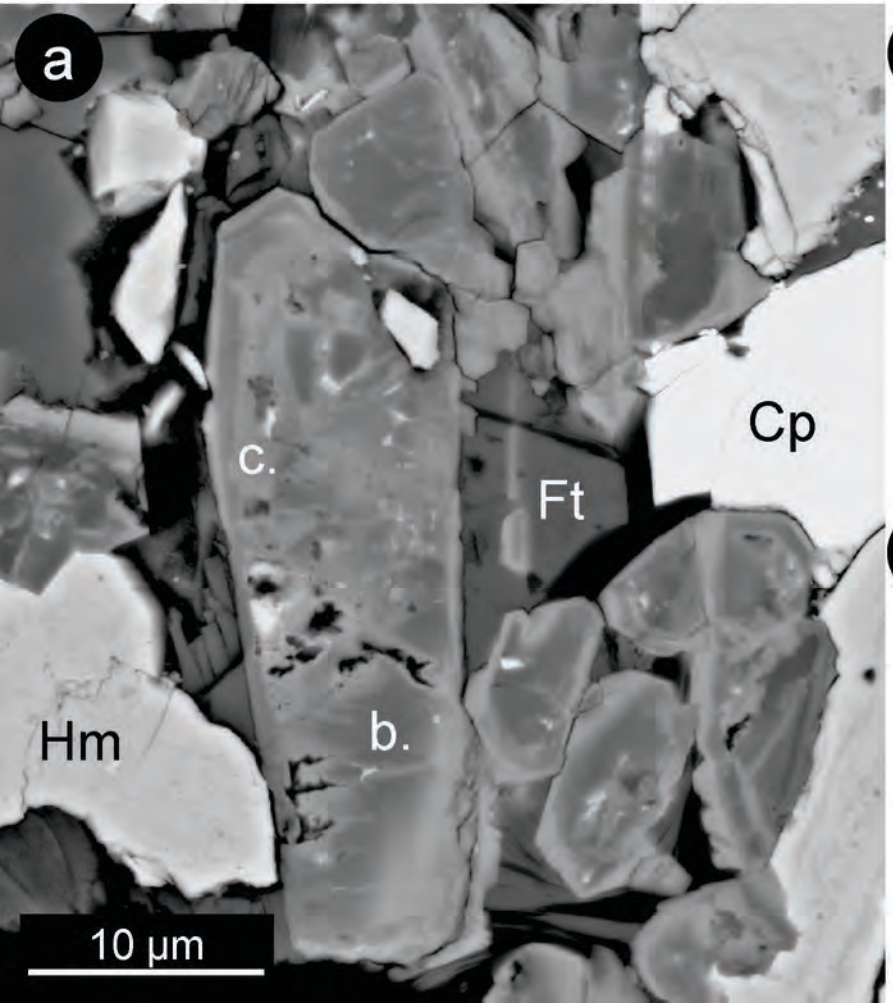
a
c.
Ft
Cp
Hm
b.
10 µm

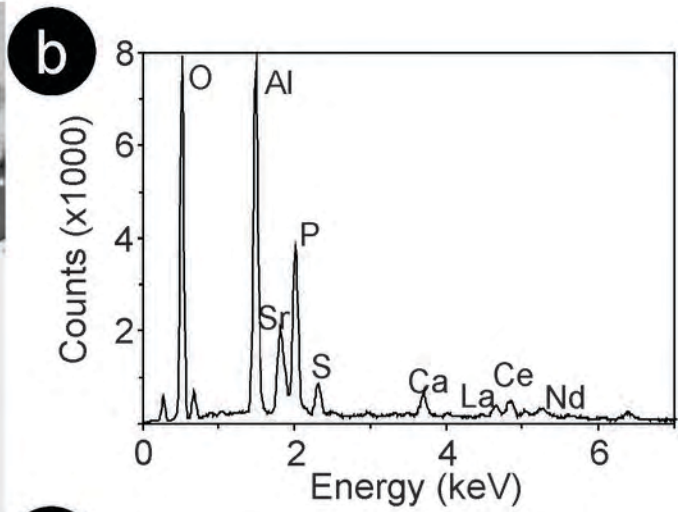
b
Counts (x1000)
Energy (keV)
O
Al
P
Sr
S
Ca
La
Ce
Nd

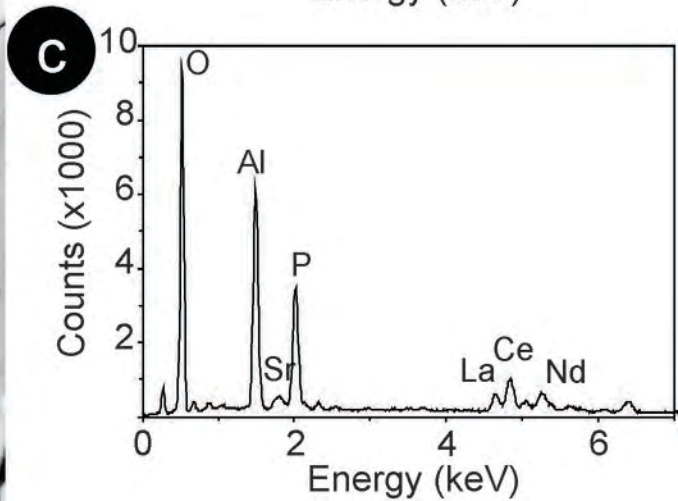
c
Counts (x1000)
Energy (keV)
O
Al
P
Sr
La
Ce
Nd

Figure 5

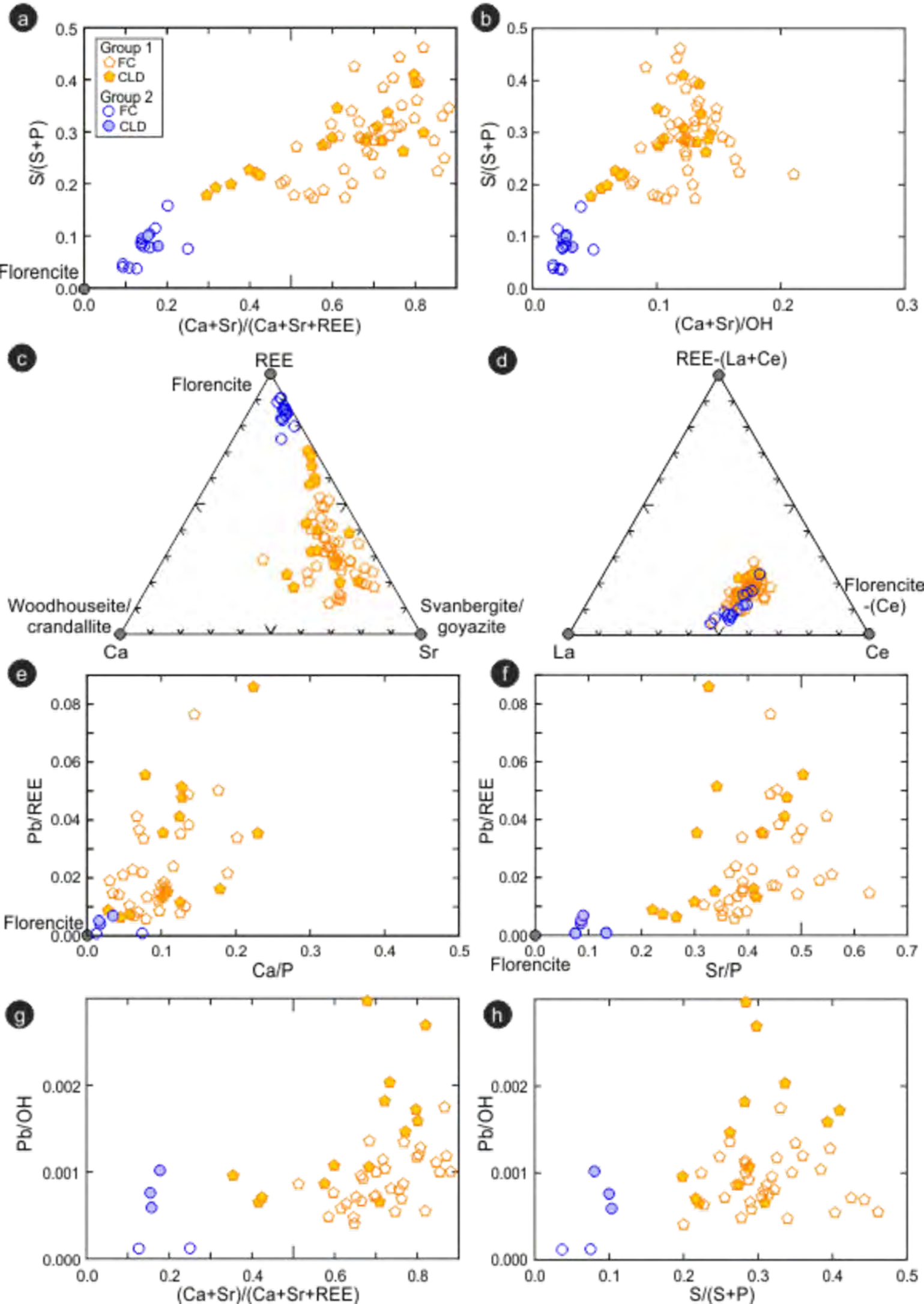
a
Group 1
FC
CLD
Group 2
FC
CLD
S/(S+P)
Florencite
(Ca+Sr)/(Ca+Sr+REE)
b
S/(S+P)
(Ca+Sr)/OH
c
REE
Florencite
Woodhouseite/
crandallite
Svanbergite/
goyazite
Ca
Sr
d
REE-(La+Ce)
Florencite
-(Ce)
La
Ce
e
Pb/REE
Florencite
Ca/P
f
Pb/REE
Florencite
Sr/P
g
Pb/OH
(Ca+Sr)/(Ca+Sr+REE)
h
Pb/OH
S/(S+P)

Figure 6

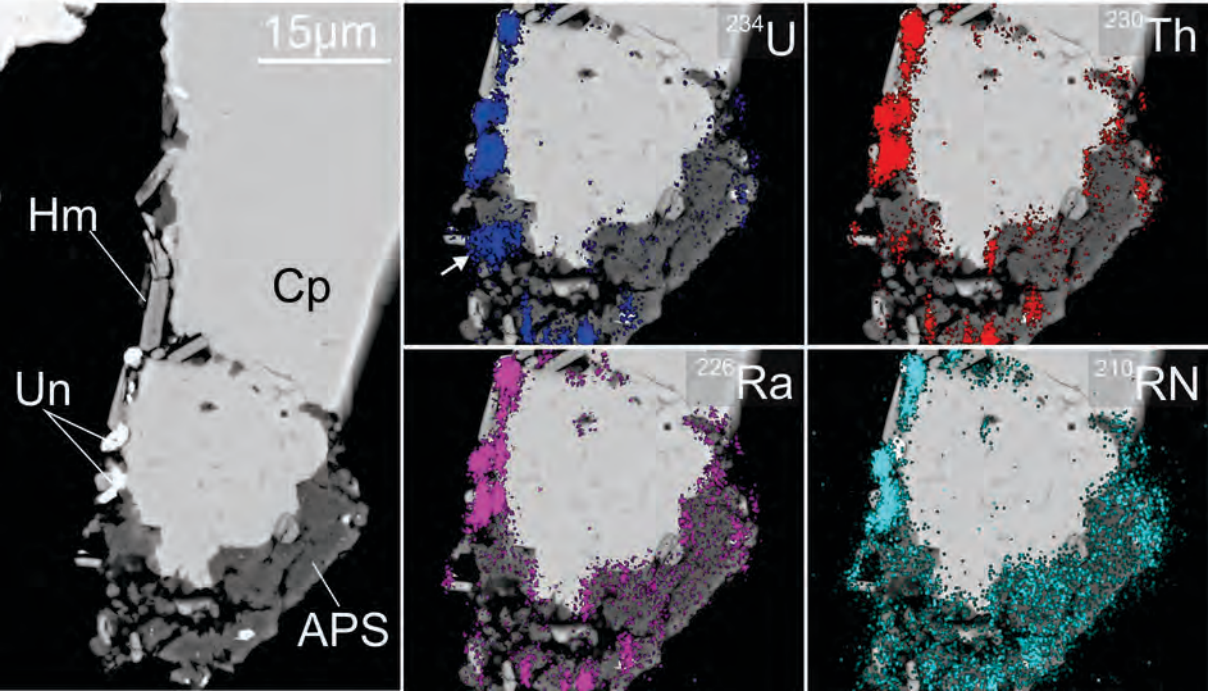

Figure 7

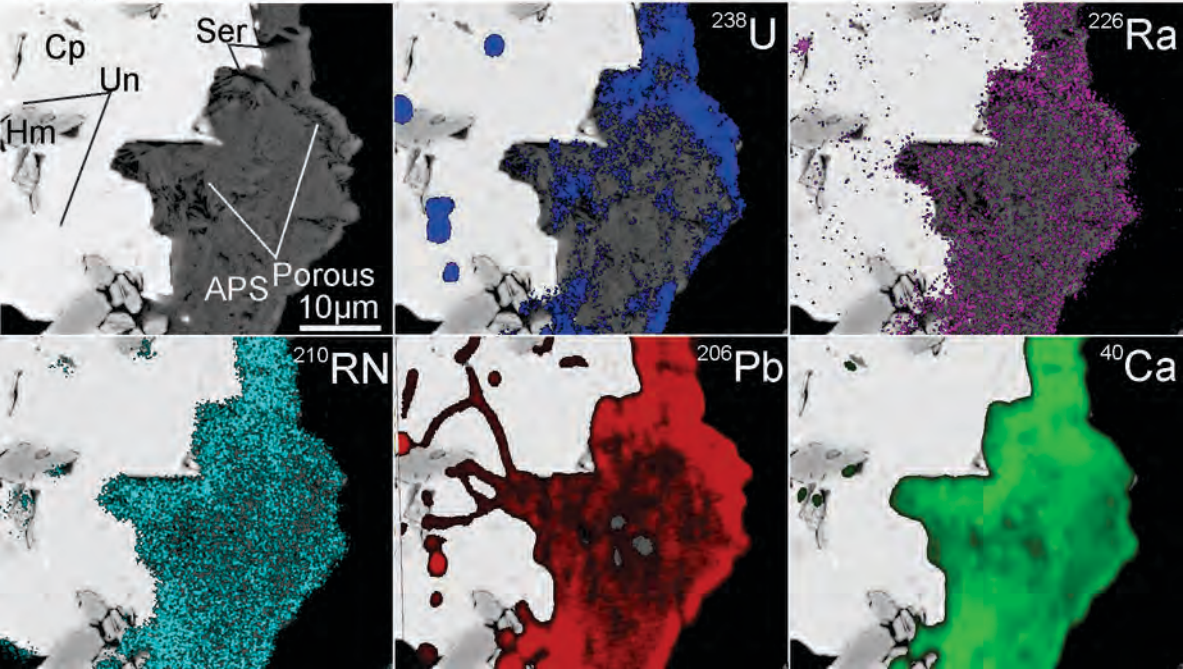

Figure 8

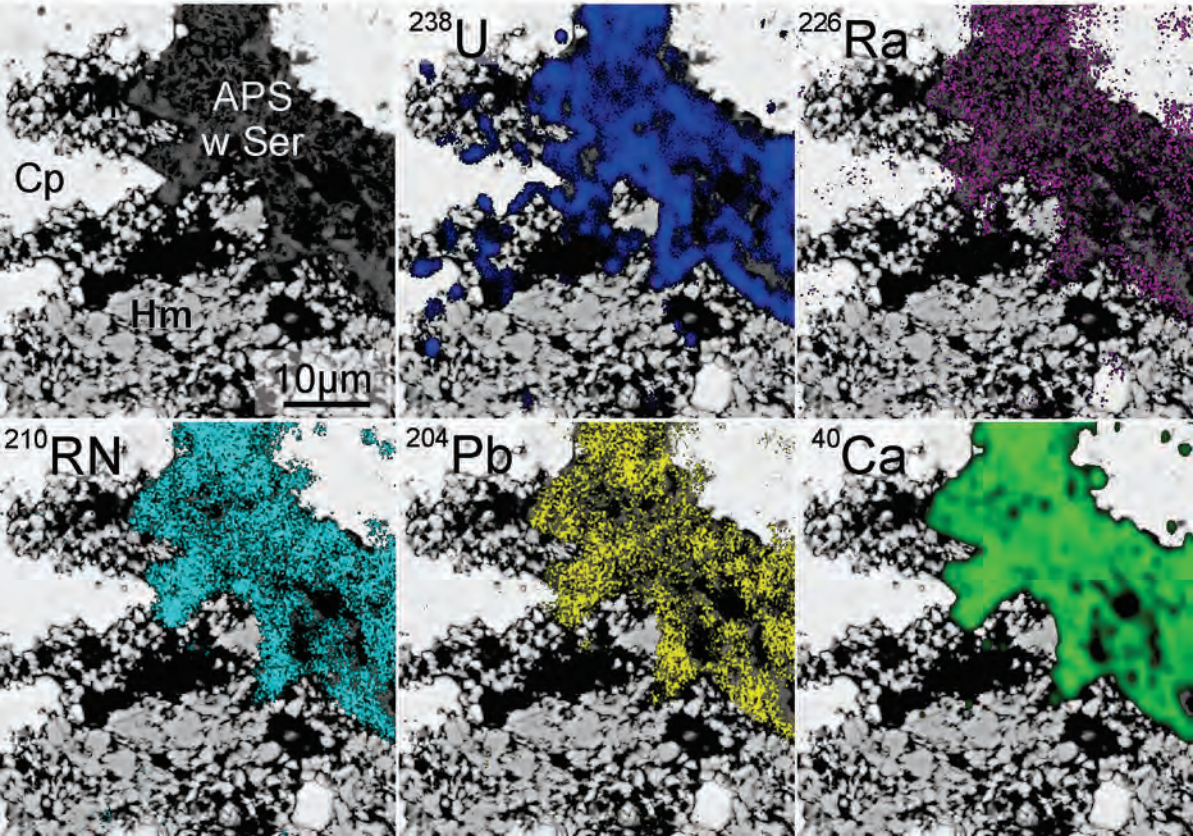

Figure 9

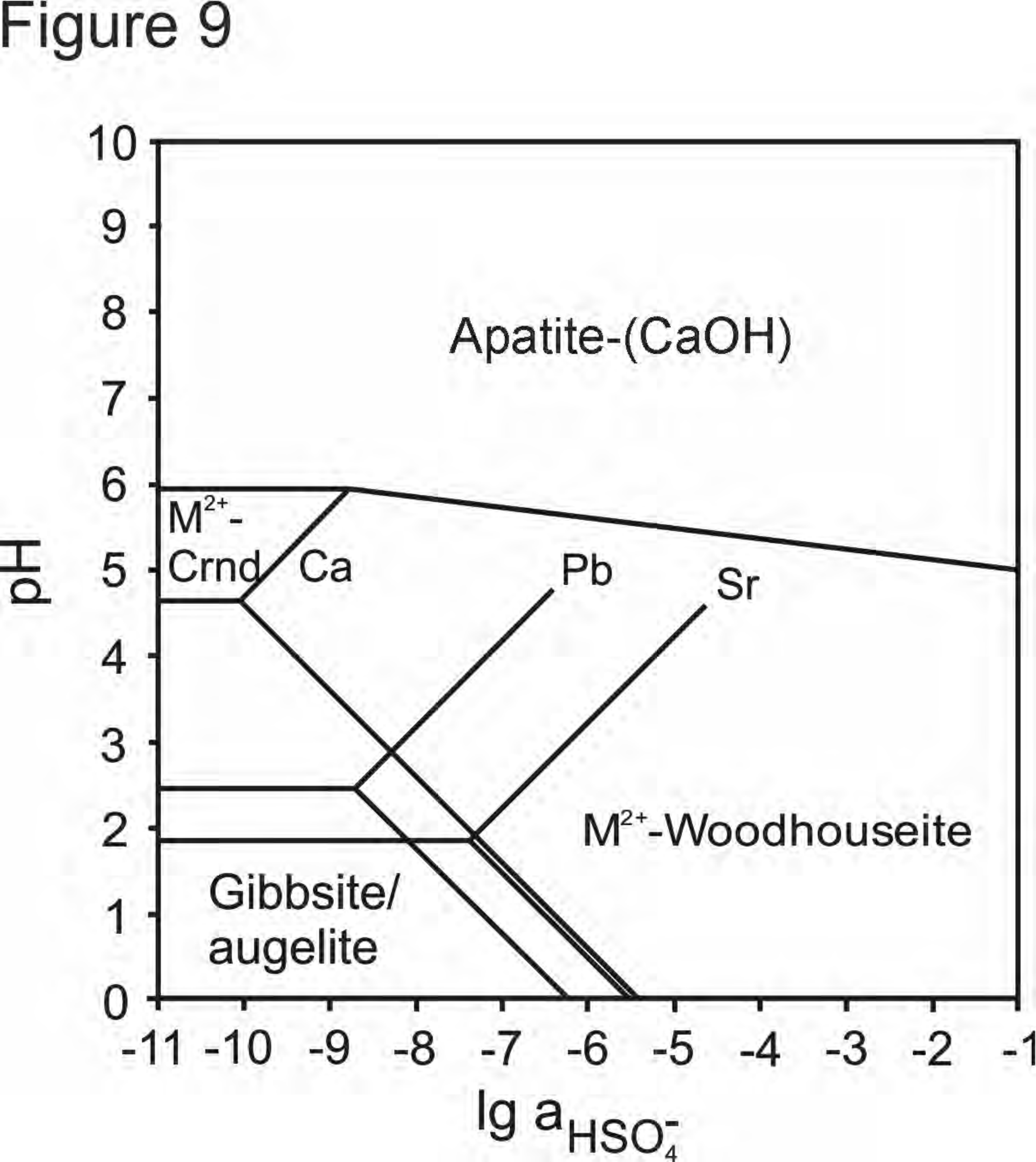
10
9
8
7
6
5
4
3
2
1
0
pH
Apatite-(CaOH)
M^{2+}-
Crnd
Ca
Pb
Sr
M^{2+}-Woodhouseite
Gibbsite/
augelite
-11
-10
-9
-8
-7
-6
-5
-4
-3
-2
-1
lg $a_{HSO_4^-}$